Hybrid LES-RANS study on square cylinder unsteady heat transfer

X. Chen and H. Xia

Department of Aeronautical and Automotive Engineering, Loughborough University, Loughborough, United Kingdom

Abstract

Flow passing a heated square cylinder is investigated using a hybrid LES-RANS approach on unstructured grids at a moderate Reynolds number of $22,050$. The implicit SGS is applied for LES and two turbulence models are tested for near-wall RANS: the Spalart-Allmaras model and the SST k-ω model. Both models combined with the LES present good predictions of the time- and phase-averaged velocity profiles on a 4-million-cell grid. Results of the LES-SST approach agree better with the experimental data especially at locations close to the cylinder surface and this leads to improved surface convective heat transfer compared to LES-SA. Grid convergence study shows that grid resolution in the near-wall region and on the cylinder surfaces is important in resolving the unsteady convective heat transfer. Results of velocity field and surface heat transfer from the fine grid with 8 million cells compare favourably with the experimental data and show significant improvement over that of the medium and coarse grids. Analysis of turbulent statistics is performed by means of energy spectra and anisotropy invariants of the Reynolds stress tensor. Proper orthogonal decomposition (POD) is used to identify the vortex shedding phases. It is shown that the POD based phase-averaging produces more accurate velocity profiles than the conventional pressure-signal based method.

Keywords: hybrid LES-RANS, unsteady heat transfer, proper orthogonal decomposition, energy spectrum, Reynolds stress anisotropy tensor

1. Introduction

Accurate prediction of unsteady flows and the associated convective heat transfer are keys for design and optimization of industrial configurations. For applications such as gas turbine engine combustors and turbines, the flow field is highly unsteady due to the shear layer, flow separation & reattachment and oscillating wakes. These turbulent features not only are important for aerodynamic performance, but also greatly affect the convective heat transfer on solid surfaces. Therefore it is essential to have accurate prediction of both the flow field and the surface heat transfer for the purpose of evaluating and improving the performance of such components.

Experiments have been contributing to the understanding of turbulent flows and heat transfer for centuries. However, 3D structures of the flow field and surface heat transfer in some cases are difficult to access. It is also costly to set up experiments for applications such as jet engines. Hence, computational fluid dynamics (CFD) tools are now widely used for research, design and optimization of industrial applications. Reynolds-averaged Navier-Stokes equations (RANS) are the most widely used CFD tool due to its ability to provide good quality time-mean flow field and predictions on global quantities.

However, it has been suggested not suitable for the reproduction of 3D turbulent structures. For instance, the studies of Bosch and Rodi [1, 2] indicated that unsteady RANS failed to reproduce details of the 3D turbulent structures in flow passing a square cylinder although the Strouhal number, lift and drag coefficient were well-predicted. Its performance in estimating the surface heat transfer was far from satisfactory due to the missing details of vortices close to the cylinder surfaces. Large-eddy simulation (LES) has been receiving increasing attention in the study of highly unsteady flows in recent decades because of its ability in resolving the unsteady vortices. Studies of Rodi et al. [3] and Wiesche [4] shown that the 3D turbulent structures near the cylinder surfaces and in the wake can be accurately captured using LES on structured grids. It was also shown by Boileau et al. [5] that the convective heat flux on surfaces of a heated square cylinder in cross flow can be accurately predicted using a fully wall resolved LES on a 12.5-million-cell unstructured grid with the use of an explicit subgrid-scale (SGS) model. It is worth noting that the grid points required for fully wall-resolved LES in the near-wall region is proportional to Re^2, nearly as many as for direct numerical simulation (DNS). This makes the wall-resolved LES very expensive, especially for high Reynolds number. On the contrary, using a wall function to model the near-wall effects is significantly cheaper. But Boileau et al. [5] found out that the wall-function LES failed to produce acceptable prediction for surface heat transfer.

In recent years, more attention has been paid combining RANS and LES together. Spalart et al. [6] first proposed the concept of detached eddy simulation (DES) to study massively separated flows. The DES attempts to combine the advantages of LES in resolving vortices away from the wall with well-developed RANS models in the near-wall region to reduce computational expenses. A number of successful studies using DES have been carried out since then [7, 8, 9]. In particular, Barone & Roy [10] successfully applied DES in the study of the turbulent wake of a square cylinder with structured grids. In all the studies above, the Spalart-Allmaras (SA) turbulence model is adopted and promising results are obtained. However, the RANS/LES interface is strongly dependent of the grid spacing near the wall. In the present study, we focus on a hybrid LES-RANS approach for unstructured grids based on wall proximity. The RANS/LES interface is hence determined in the boundary layer at a given dimensionless wall distance (y^+). Davison and Peng [11] were the first to explore this approach. In their study, the k-l SGS model is used with a k-ω near-wall RANS approach. Encouraging results were obtained for a fully developed channel flow and a hill flow. Attempts to reduce the model complexity by using only the k-l based model for the whole domain are performed by Tucker and Davison [12] for channel flows and Tucker [13] for jet flows and noise. This hybrid LES-RANS has also been successfully applied to noise prediction of chevron jet flows [14, 15] using implicit LES combined with the near-wall SA RANS model. In the present study, the hybrid LES-RANS approach is adopted and two RANS models are tested for the near-wall region: the one-equation SA model and two-equation SST k-ω model. The RANS and LES regions are blended based on a modified wall distance $\widetilde{d}$ using a smooth analytic function. Grid convergence studies have been performed on different near-wall resolutions.

In the sections below, details of the hybrid LES-RANS solver are explained first. Configuration of the present study is introduced in section 3 with detailed flow conditions, the meshing strategy and reference experiments for validation. Section 4 presents the analysis of results, which is divided into 4

parts. The first part presents the comparison and analysis of the time-averaged and fluctuating velocity and surface heat transfer results. The second part illustrates the phase-averaged velocity and surface heat transfer profiles and evaluation of their fluctuation. Analysis is carried out to associate the phase-variation of local surface heat transfer results with the vortex shedding phenomenon. The third part provides the analysis of turbulent statistics in regions of interest with the help of the energy spectra and the anisotropic invariants map (AIM) of the Reynolds stress tensor. The last part illustrates an improved phase identification of the vortex shedding using proper orthogonal decomposition (POD).

2. Numerical method

The Favre-averaged compressible Navier-Stokes equations for ideal gas are solved in conservation form,

$$\frac{\partial \overline{\mathbf{Q}}}{\partial t} + \frac{\partial \overline{\mathbf{F}}_i^{inv}}{\partial x_i} - \frac{\partial \overline{\mathbf{F}}_i^{vis}}{\partial x_i} = 0 \tag{1}$$

The conservative variables are $\overline{\mathbf{Q}} = [\overline{\rho}, \overline{\rho}\widetilde{u}_i, \widetilde{E}]^T$, the inviscid and viscous fluxes are defined as $\overline{\mathbf{F}}_i^{inv} = \widetilde{u}_i\overline{\mathbf{Q}} + [0, \delta_{1i}\overline{p}, \delta_{2i}\overline{p}, \delta_{3i}\overline{p}, \widetilde{u}_i\overline{p}]^T$ and $\overline{\mathbf{F}}_i^{vis} = [0, \widetilde{\tau}_{1i}, \widetilde{\tau}_{2i}, \widetilde{\tau}_{3i}, \widetilde{\tau}_{ki}\widetilde{u}_k + \widetilde{q}_i]^T$. The stress tensor $\widetilde{\tau}_{ij}$, total energy $\widetilde{E}$ and heat flux $\widetilde{q}_j$ satisfies,

$$\widetilde{\tau}_{ij} = 2(\mu + \mu_T)\left(\widetilde{S}_{ij} - \frac{1}{3}\partial_k\widetilde{u}_k\delta_{ij}\right), \qquad \widetilde{E} = \overline{\rho}\widetilde{e} + \frac{1}{2}\overline{\rho}\widetilde{u}_i\widetilde{u}_i, \qquad \widetilde{q}_i = -(\kappa + \kappa_T)\frac{\partial \widetilde{T}}{\partial x_i} \tag{2}$$

where the turbulent thermal conductivity is computed from $\kappa_T = \mu_T c_p/Pr_T$. An extra equation of state $\overline{p} = \overline{\rho}R\widetilde{T}$ is also included.

2.1. Near-wall modelling

In the one-equation SA model [16], the turbulent eddy viscosity is defined as $\mu_T = \overline{\rho}\widetilde{\nu}f_{\nu 1}$, where $\widetilde{\nu}$ satisfies the transport equation,

$$\frac{\partial \widetilde{\nu}}{\partial t} + \widetilde{u}_i\frac{\partial \widetilde{\nu}}{\partial x_i} = c_{b1}\widetilde{S}\widetilde{\nu} - c_{w1}f_w\left(\frac{\widetilde{\nu}}{d}\right)^2 + \frac{1}{\delta}[\nabla\cdot((\nu+\widetilde{\nu})\nabla\widetilde{\nu}) + c_{b2}(\nabla\widetilde{\nu})^2] \tag{3}$$

where $f_{\nu 1},\ c_{b1},\ c_{b2},\ c_{w1},\ f_w$ are coefficients and functions following the original definition of Ref. [16].

The SST k-ω model is also tested as the near-wall model. The turbulent eddy viscosity μ_T reads,

$$\mu_T = \frac{\overline{\rho}\alpha_1 k}{max\left(\alpha_1\omega, \Omega F_2\right)} \tag{4}$$

in which the turbulent kinetic energy k and specific dissipation rate ω satisfy two transport equations,

$$\frac{\partial k}{\partial t} + \frac{\partial \widetilde{u}_i k}{\partial x_i} = \widetilde{P}_k - \frac{k^{3/2}}{L_T} + \frac{\partial}{\partial x_i}\left[(\nu + \sigma_k\nu_T)\frac{\partial k}{\partial x_i}\right] \tag{5}$$

$$\frac{\partial \omega}{\partial t} + \frac{\partial \widetilde{u}_i \omega}{\partial x_i} = \left(\frac{\alpha}{\nu_t}\right)\widetilde{P}_k - \beta\omega^2 + \frac{\partial}{\partial x_i}\left[(\nu + \sigma_\omega\nu_T)\frac{\partial \omega}{\partial x_i}\right] + 2(1-F_1)\frac{\sigma_{\omega_2}}{\omega}\frac{\partial k}{\partial x_i}\frac{\partial \omega}{\partial x_i} \tag{6}$$

where $L_T = \sqrt{k}/\beta^*\omega$ is the turbulent length scale, all coefficients and functions such as $\widetilde{P}_k$, Ω, F_1, F_2, α, α_1, β, β^*, σ_k, σ_ω, σ_{ω_2} follow the definition of Ref. [17].

The SST k-ω model is well-known for combining the accuracy of Wilcox's k-ω model in resolving the near wall boundary layer and the low free-stream sensitivity of the Jones-Launder k-ε model. Additionally, Bradshaw's assumption of the principal shear-stress is considered for extra ability to solve flows with adverse pressure gradients [18].

2.2. LES-RANS hybridization

The RANS and LES regions are blended by a modification of the nearest wall distance d in the SA model and turbulent length scale L_T in the SST model. In the present study, the modified wall distance $\widetilde{d}$ is defined as,

$$\widetilde{d} = \left[1 - \tanh\left(a_1 \frac{d - d_c}{d_c}\right)\right] \frac{d}{2} \tag{7}$$

where a_1 is the parameter to control the decay rate of $\widetilde{d}$ in the mixed zone, d_c is the RANS cut-off distance typically at $y^+ \sim 60$. As Figure 1 shows, the RANS and LES regions are defined based on the modified wall distance $\widetilde{d}$. It controls the RANS model, so that the turbulent eddy viscosity vanishes in the LES region. In addition, $\varepsilon = \tanh\left[a_2(d - \widetilde{d})\right]$ is a weighting parameter for LES if an explicit SGS model is used and the parameter a_2 controls the growth of ε in the mixed zone. A smooth transition in the eddy viscosity field is therefore obtained and helps maintain good numerical stability. An example of the turbulent viscosity profile from the near-wall RANS above the cylinder top surface is presented in Figure 2. No explicit SGS model is used ($\varepsilon = 0$) in the present study, which is often referred to as implicit or numerical LES.

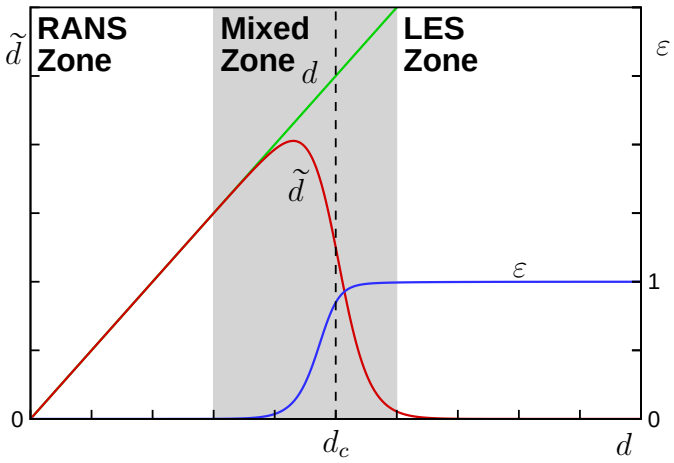

Figure 1: Blending of RANS and LES regions.

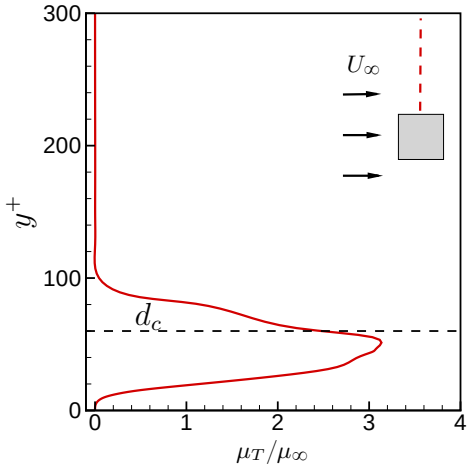

Figure 2: Turbulent viscosity of near-wall RANS model above the cylinder top surface.

2.3. Spatial and temporal discretization

Viscous terms are discretized using the central differencing scheme while a MUSCL reconstruction with a modified Roe's scheme is used for inviscid fluxes at the common face of two neighbour cells,

$$\mathbf{F} = \frac{1}{2}(\mathbf{F}_L + \mathbf{F}_R) - \frac{\gamma}{2}\left|\frac{\partial \mathbf{F}}{\partial \mathbf{Q}}\right|(\mathbf{Q}_R - \mathbf{Q}_L) \tag{8}$$

where the up-winding term is controlled by parameter $\gamma \in [0.1, 1]$, $\mathbf{Q}$ and $\mathbf{F}$ are the conservative and flux vectors. Subscripts L and R represent the immediate left and right position of the common flux face, where piecewise linear reconstructions are performed from cell centres to give a second-order spatial accuracy. Moreover, the dual-time advancing is employed with the outer physical time discretized by a three-level backward Euler scheme, thus leading to a second-order temporal accuracy. The inner pseudo time is advanced by a three-stage Runge-Kutta scheme. As the outer time is discretized implicitly, it allows larger physical time steps to increase the efficiency compared with explicit time marching [19].

3. Configuration

3.1. Geometry and physical conditions

In the present study, the diameter (side length) of the cylinder is set as $D = 1\ cm$. The corresponding Reynolds number is $Re_D = 22,050$. The computational domain is 14 D in height, 27 D in length and 4 D in span, which maintains the same blockage ratio as the experiment of Lyn & Rodi [20]. The conditions of inflow are set to $p_\infty = 101,325\ Pa$, $T_\infty = 300\ K$ and $M_\infty = 0.108$. The top, bottom and side surfaces of the flow domain are treated as slip walls, while a no-slip and isothermal wall boundary of $T_{wall} = 330\ K$ is applied to the cylinder surfaces. The temperature difference between the wall and the free-stream induces a variation of fluid properties in the near-wall boundary layer. Therefore, the Reynolds number of the present study is calculated based on a film temperature of $T_f = \frac{1}{2}(T_\infty + T_{wall}) = 315\ K$.

100 *3.2. Meshing strategy*

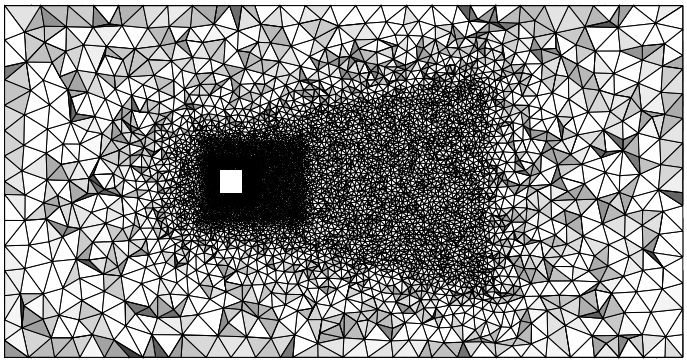

(a) Cut-away view of the volume cells.

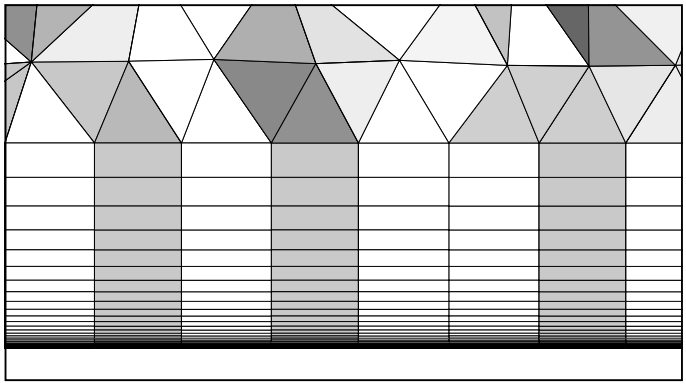

(b) An enlarged view of the near-wall cells and prism layers.

Figure 3: The 4-million-cell unstructured grid.

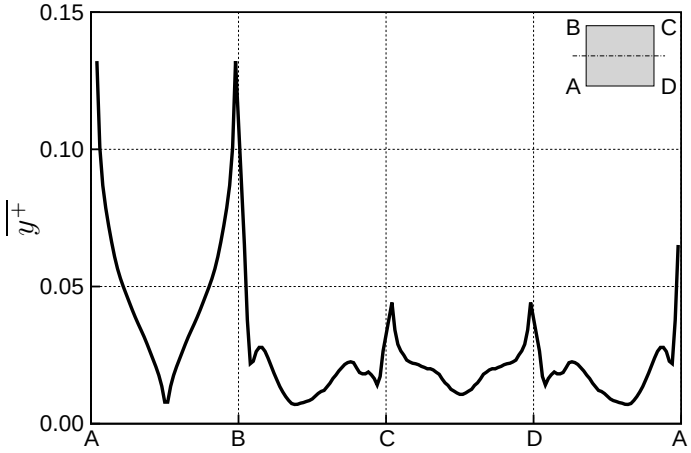

Figure 4: Time-averaged wall y^+ profile.

An unstructured grid of about 4 million cells is shown in Fig. 3. The near wall region, near and far wake downstream the cylinder are refined to better resolve the flow separation & reattachment near the cylinder surfaces and the vortex shedding in the wake. Fig. 3b illustrates the near-wall prismatic cells in an enlarged view. The first cell height of the prism layers is set to 10^{-4} D and the corresponding $\overline{\Delta y^+}$

value on cylinder surfaces is plotted in Fig. 4. The near-wall resolution is limited to $\overline{\Delta y^+} \ll 1.0$ by the current first cell height, while $\overline{\Delta x^+} \approx 2.7$ and $\overline{\Delta z^+} \approx 4.7$ for the surface cells. The effect of the wall is fully resolved by the near-wall models without the use of a wall function under current $\overline{\Delta y^+}$.

A reduced grid resolution on cylinder surfaces and in the near-wall region is applied to generate a coarser grid with roughly 1 million cells, whereas increased grid resolution is applied to the same regions for a finer grid with over 8 million cells. The surface grid spacing near the 4 corners is reduced in the 8-million-cell grid in order to capture the flow crossing the corners more accurately. The first cell height and the total height of the prism layers are kept the same in the 3 grids. Grid convergence study is performed on the 1-million-cell, 4-million-cell and 8-million-cell grids by validating the velocity field and surface heat transfer results. A summarise of the cases being discussed in the present study is presented in Table 1, in which N_{cell} is the total cell number, N_{prism} the total number of the prism layers, λ_{prism} the prism layer growth rate, Δt the time step size and T_{total} the total physical time. The convective time is defined as $t^* = D/U_\infty$.

Table 1: Simulations of the present study.

Case	SGS model	Near wall RANS	N_{cell}	N_{prism}	λ_{prism}	$t^*/\Delta t$	T_{total}/t^*
1M$k\omega$	Implicit	SST k-ω	1,110,195	28	1.2	2000	110
4MSA	Implicit	SA	4,462,916	27	1.2	2000	110
4M$k\omega$	Implicit	SST k-ω	4,462,916	27	1.2	2000	110
8M$k\omega$	Implicit	SST k-ω	8,806,698	28	1.16	2000	110

3.3. Reference experiments and data processing method

Several experimental studies are selected for the validation of flow field and surface heat transfer results. Lyn and Rodi [20] and Lyn et al. [21] investigate the velocity field near the cylinder top surface and in the wake using laser Doppler velocimetry (LDV). Both time- and phase-averaged velocities and their fluctuations are provided. Fohanno & Martinuzzi [22] also show some velocity data measured by phase Doppler anemometry (PDA). Results of the pressure coefficient on cylinder surfaces are obtained from Igarashi [23] at $Re = 37,000$ and Bearman & Obasaju [24] at $Re = 20,000$. The global Strouhal number is available from Lyn et al. [21] and Bearman & Obasaju [24] as a reference of the vortex shedding frequency. According to Lyn et al. [21], this frequency is obtained from the fast Fourier transform (FFT) of the pressure signal taken from the centreline of the cylinder top surface. The signal is also used for phase identification of the vortex shedding.

The instantaneous flow variable $f(\mathbf{x}, t)$ can be decomposed into a time-averaged component and a fluctuating component, or a phase-averaged component and a fluctuating component,

$$f(\mathbf{x}, t) = \overline{f}(\mathbf{x}) + f'(\mathbf{x}, t) = \langle f(\mathbf{x}, \varphi) \rangle + f(\mathbf{x}, t)'' \tag{9}$$

where φ is the phase angle with regards to to the vortex shedding period. Root-mean-square (RMS) value of the fluctuating components is used for the validation of velocity fluctuations. The phase-averaged part

is obtained by averaging datasets that belong to the same phase angle. Following Lyn & Rodi [20], phase angle of each dataset is defined using the pressure signal $p(t)$ from the centreline of cylinder top surface. This pressure signal is then processed through a second-order low-pass Butterworth filter [25], whose cutting frequency is equal to the vortex shedding frequency. The peaks and valleys of the filtered signal
135 are used to anchor every half of the vortex shedding period. 10 discrete phase angles are selected in every half period, resulting in 20 phases per vortex shedding cycle. Fig. 5 shows an example of the phase angles on the filtered pressure signal. Spanwise-averaging is also applied to the dataset of the flow field as well as on cylinder surfaces. A sketch of the 2D positions for velocity validation is shown in Fig. 6.

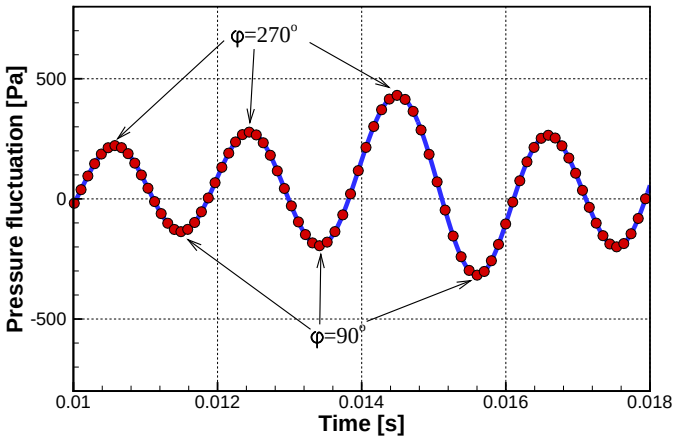

Figure 5: Definition of phase angles on filtered pressure signal. —— filtered signal, ● selected phase angles.

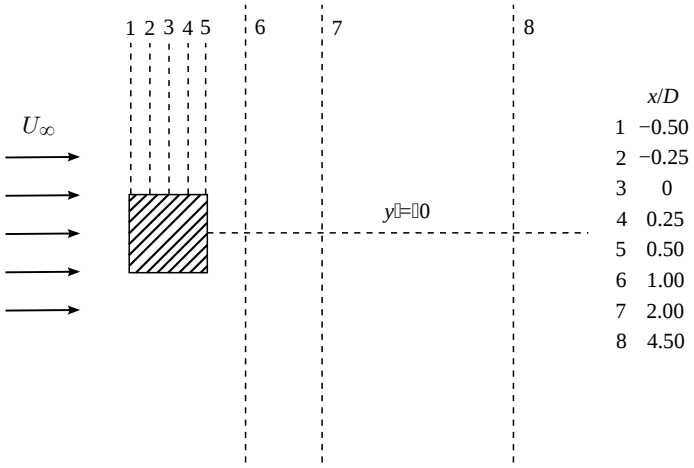

Figure 6: 2D probe positions of the velocity profiles.

For the validation of surface heat transfer, Igarashi [23] measures time-averaged global and local Nusselt number on cylinder surfaces at different Reynolds numbers. An empirical correlation is proposed by Igarashi [23] for the relation between global Nusselt number and Reynolds number,

$$\overline{Nu}_g = 0.14 Re^{0.66} \tag{10}$$

which is valid for $5000 < Re < 60000$. As none of Igarashi's results are at the present Reynolds number ($Re = 22,050$), this correlation is transformed to scale the global and local Nusselt number from the

closest Reynolds number ($Re = 18,500$) for comparison,

$$\overline{Nu}_{scaled} = \overline{Nu}_{exp}(\frac{Re_{sim}}{Re_{exp}})^{0.66} \tag{11}$$

Yoo et al. [26] measure the mass transfer of flow passing a square cylinder using the naphthalene-sublimation technique. The local Sherwood number on cylinder surfaces is used to calculate the corresponding local Nusselt number by using an analogy between heat and mass transfer: $Nu = Sh(Pr/Sc)^{1/3}$. The Prandtl number of the experiment is $Pr = 0.71$ and the Schmidt number is $Sc = 2.53$. Those data are obtained from the correlation of Cho et al. [27] taken at the same temperature of Yoo et al.'s experiment.

A short summary of the global quantities in the experiments mentioned above is presented in Table 2, where the turbulence intensity Tu is measured at the position of the cylinder in its absence. The turbulence intensity of the experiments, especially in the heat and mass transfer cases of Igarashi [23] and Yoo et al. [26], is at a low level ($< 1\%$), so free-stream turbulence is not modelled in the current simulations.

Table 2: A summary of the global quantities in experiments.

Data source	Re	St	Tu
Lyn & Rodi [20]	21400	0.134	2%
Lyn et al. [21]	21400	0.132 ± 0.004	2%
Fohanno & Martinuzzi [22]	18500	0.132 ± 0.003	$< 3\%$
Bearman & Obasaju [24]	20000	0.13	$< 0.04\%$
Igarashi [23]	37000	0.14	$< 0.5\%$
	18500	N/A	$< 0.5\%$
Yoo et al. [26]	22500	N/A	$< 0.5\%$

4. Results and discusstions

Fig. 7 shows the instantaneous flow field and temperature field of the 8M$k\omega$ case. The turbulent structures are clearly illustrated by the isosurfaces of λ_2 criterion [28] in Fig. 7a. Shear layers are formed above and below the cylinder top and bottom surfaces respectively. Highly unsteady structures occur not far downstream the front surface and stay energetic in the near and intermediate wake. Small vortices can also be found close to the cylinder surfaces. These unsteady flow structures strongly affect the convective heat transfer on cylinder surfaces as Fig. 7b shows. The flow reattaches on the rear surface due to the wake vortices generated by flow separation. Heat is brought away by the reattaching flow rapidly so that the flow temperature near the rear surface stays low except the small recirculation region near the top/bottom corner. Reattaching flow consists of separation from the shear layer and reverse flow from the wake sweep on the top/bottom surfaces from downstream to upstream. However, this recirculation is limited inside the shear layer region. A clear boundary is formed above and underneath the top and bottom surfaces between the high temperature reattaching flow and the low temperature free-stream.

This results in a stall region of the high temperature flow close to the front corner. It is expected that the heat transfer rate on the top/bottom surface reduces from downstream to upstream. A valley on the surface heat transfer profile is expected close to the front corner of the top/bottom surface while a peak will appear near the rear corner. Moreover, the rear surface will have a relatively high heat transfer rate compared to that on the top/bottom surface. On the front surface, the heat transfer rate will stay low near the stagnation point and increase towards the corner as the flow attached to the surface accelerates from the stagnation point to the corner.

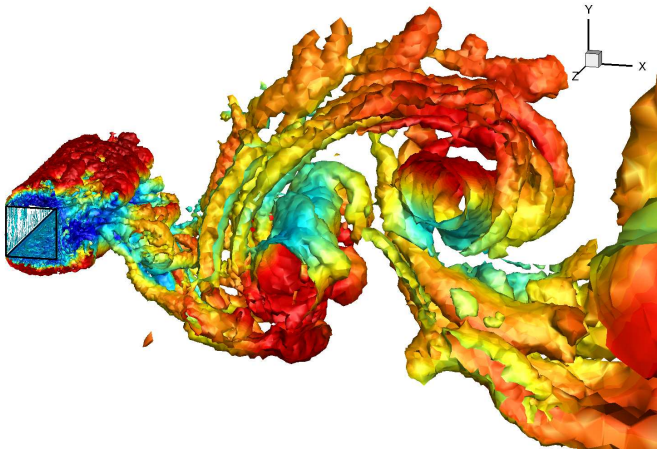

(a) Vortices visulized by isosurfaces of λ_2 and coloured by velocity u.

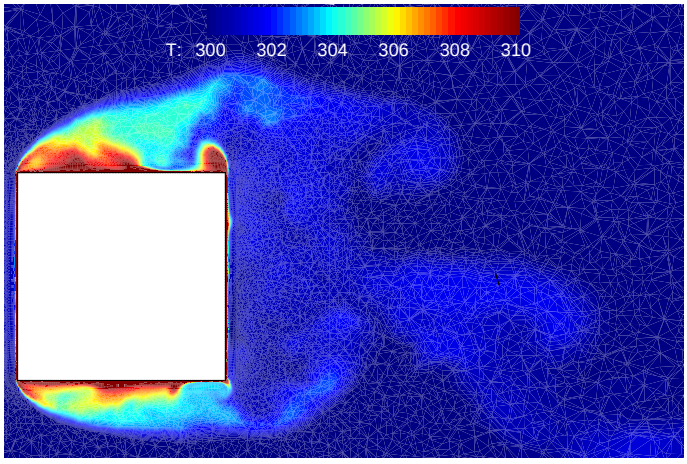

(b) Contours of temperature near the cylinder on the central slice.

Figure 7: Visulization of the instantaneous flow field at $t = 0.0032s$ in the 8M$k\omega$ case.

4.1. Time-averaged results

4.1.1. Time-averaged surface pressure coefficient

The pressure field around the cylinder is closely related to the velocity field attach to the wall. Fig. 8 illustrates the time-averaged pressure coefficient profiles on cylinder surfaces. Profiles of all cases match the experimental data quite well on the front surface. Discrepancies can be observed on the top, bottom and rear surfaces between profiles of the 4MSA case and the experiments, while results of other cases agree well with that of the experiments. The higher pressure coefficient predicted by the 4MSA

case reveals that the kinetic energy of the reattaching flow near the top, bottom and rear surfaces is underpredicted. This will potentially lead to a lower convective heat transfer rate in the corresponding regions. Slight overestimate on the top/bottom surface close to corner C and D can be found in results of the 1M$k\omega$ case, while improved results are presented by case 4M$k\omega$ and 8M$k\omega$. Further improvement is obtained especially near the corner in the 8M$k\omega$ case as a result of increased near-wall resolution and reduced surface grid spacing near the corners.

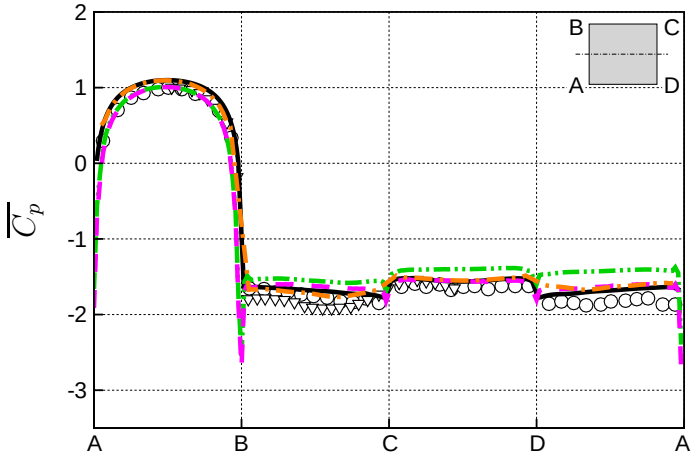

Figure 8: Time-averaged pressure coefficient profiles. −·− 1M$k\omega$, −··− 4MSA, − − 4M$k\omega$, —— 8M$k\omega$, ○ Igarshi [23], ▽ Bearman & Obasaju [24].

4.1.2. Time-averaged velocity profiles

Fig. 9 shows the time-averaged and fluctuating streamwise velocity at 5 different locations above the cylinder top surface. Profiles of all cases agree with the experimental data on both the time-averaged and RMS fluctuation part. The upper bound of the shear layer, where the maximum velocity is reached, has been accurately captured by case 4MSA, 4M$k\omega$ and 8M$k\omega$. The recovery of time-averaged velocity across the shear layer is underestimated in the 1M$k\omega$ case, resulting in a higher position of the shear layer's upper bound. Improved prediction of the time-averaged velocity profiles across the shear layer near the front corner ($x/D < -0.25$) is provided by the 8M$k\omega$ case due to increased grid resolution. A very small underestimate of the time-averaged velocity occurs in the reverse flow region downstream ($x/D > 0$) in all cases. For the fluctuation profiles, a much clearer peak close to the wall in the downstream region ($x/D > 0$) is illustrated by the 8M$k\omega$ case compared to case 4MSA and 4M$k\omega$. It shows that the reverse flow in the near-wall region is fluctuating due to the recirculation flow from the unsteady wake. A strong peak occurs at the position of the shear layer's upper bound and the width increases when moving towards downstream. This is because of the flapping movement of the shear layer in response to the vortex shedding in the wake.

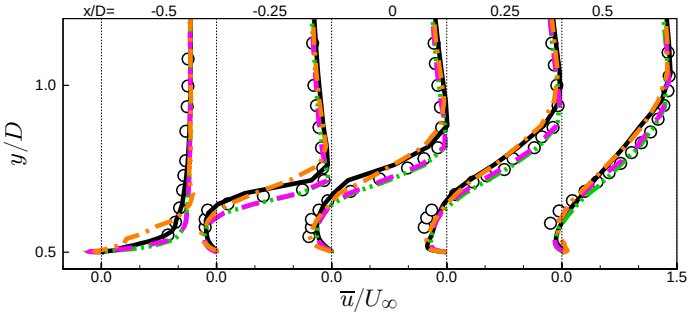

(a) Time-averaged velocity u

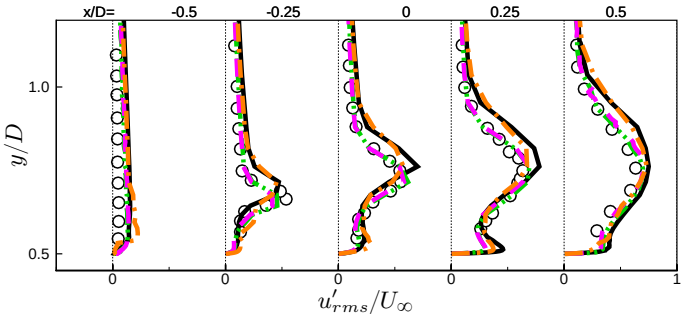

(b) RMS fluctuation of velocity u

Figure 9: Time-averaged streamwise velocity and fluctuation profiles above the cylinder. −·− 1M$k\omega$, −··− 4MSA, – – 4M$k\omega$, —— 8M$k\omega$, ○ Lyn & Rodi [20].

The recovery of the time-averaged streamwise velocity and fluctuation in longitudinal direction ($y = 0$) after the cylinder reflects the influence of the wake vortex shedding to some extent. Fig. 10 illustrates the time-averaged streamwise velocity and its RMS fluctuation of the 4 cases. Overall, profiles of case 4M$k\omega$ and 8M$k\omega$ are much closer to that of the experiments compared to that of case 1M$k\omega$ and 4MSA. For the time-averaged streamwise velocity recovery, case 1M$k\omega$ and 4MSA overestimate the recovery speed in the near-wake region ($x/D \in (1, 4)$). The 8M$k\omega$ case shows a slightly lower recovery speed and better agreement to experimental data compared to the 4M$k\omega$ case because of the refined grid resolution in spite of a small underprediction of the reverse flow velocity. This reveals that the decay of the vortex kinetic energy in x direction in the wake is overpredicted in case 1M$k\omega$ and 4MSA compared to that in case 4M$k\omega$, 8M$k\omega$ and experiment. This overestimate directly leads to a reduction of the reverse flow's velocity in the near wake. As a result, heat transfer on the rear surface of the cylinder will be lower and further influence on the top and bottom surfaces is also expected. For the fluctuation profiles, the 1M$k\omega$ case underestimates the peak of the fluctuation while case 4MSA, 4M$k\omega$ and 8M$k\omega$ show improved prediction. The recovery in the middle and far wake region is overpredicted by the 4MSA case compared to the 4M$k\omega$ case although a higher peak is presented. This is consistent with that observed from the time-averaged profiles.

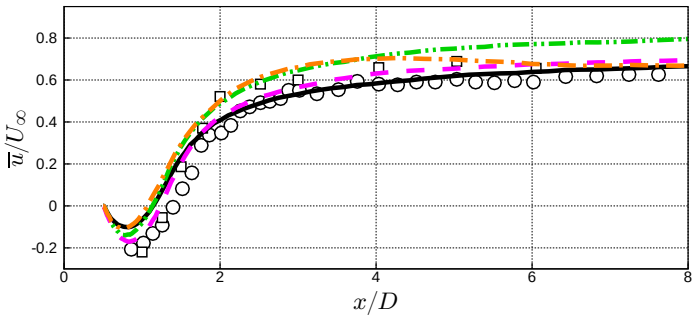

(a) Time-averaged velocity u

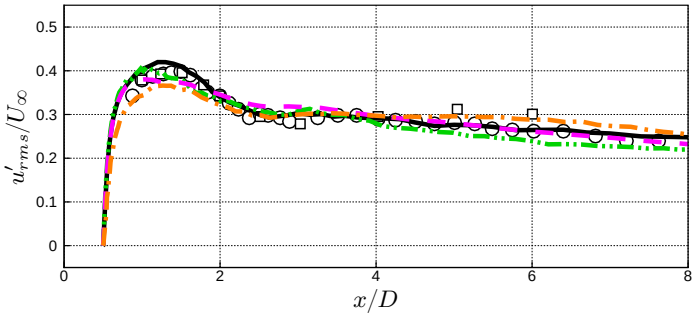

(b) RMS fluctuation of velocity u

Figure 10: Time-averaged streamwise velocity recovery and fluctuation in longitudinal direction at $y = 0$. −·− 1M$k\omega$, −·· − 4MSA, − − 4M$k\omega$, —— 8M$k\omega$, ○ Lyn et al. [21], □ Fohanno & Martinuzzi [22].

Profiles of the time-averaged streamwise velocity and its RMS fluctuation at different positions are presented in Fig. 11. Results of case 4MSA and 4M$k\omega$ agree very well with that of the experiments outside the core region of vortex shedding ($|y/D| > 1.0$). For the time-averaged profiles, the peak values in the 4M$k\omega$ case are closer to that of the experiment compared to the 4MSA case. For the fluctuation part, profiles of the 4M$k\omega$ case show slightly better agreement with the experimental profiles than that of the 4MSA case. Profiles of time-averaged transverse velocity and its RMS fluctuation in the wake are presented in Fig. 12. The time-averaged profiles of both cases agree well with the measurements. A small overestimate can be found in the fluctuation profiles of the 4MSA case, while that of the 4M$k\omega$ case agree well with the experimental data. Slight underestimate of the fluctuation profiles' peak values occurs in the downstream region ($x/D > 2$) in both cases. It suggests that the decay of the wake vortices' kinetic energy in y direction is faster in the two cases compared to that of the experiments and that in the x direction. Fig. 13 illustrates the time-averaged Reynolds stress ($\overline{u'v'}$) in the wake. Good agreement is reached between the two cases and the experiment away from the cylinder ($x/D \geqslant 2$). The Reynolds stress in the core region of the vortex shedding ($|x/D| < 0.75$) is overestimated in both cases at $x/D = 1$ although profile of the 4M$k\omega$ case shows a small improvement. This indicates that the Reynolds stress in both cases recovers slower in the near-wake region ($x/D < 1$) and faster in the middle and far wake compared to the experiment. This observation is consistent with the results of the wall-resolved LES by Boileau et al. [5].

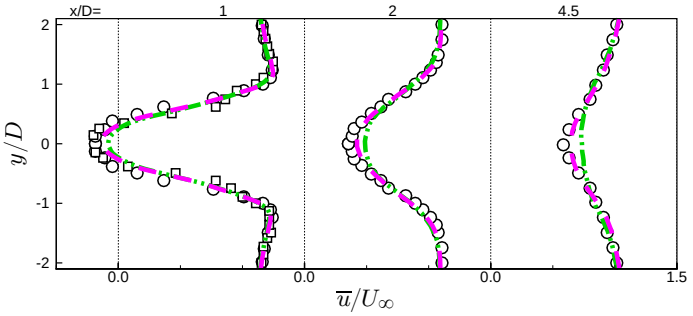

(a) Time-averaged velocity u

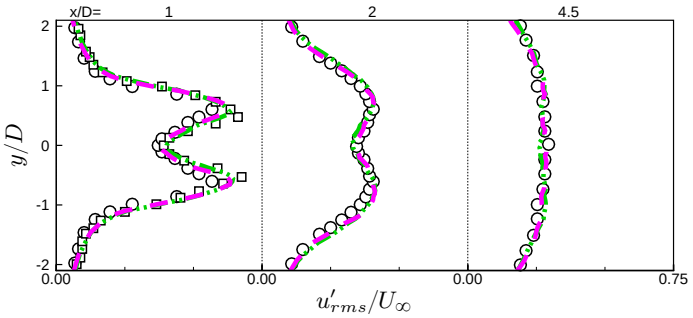

(b) RMS fluctuation of velocity u

Figure 11: Time-averaged streamwise velocity and fluctuation profiles in the wake. —··— 4MSA, – – 4M$k\omega$, ○ Lyn et al. [21], □ Fohanno & Martinuzzi [22].

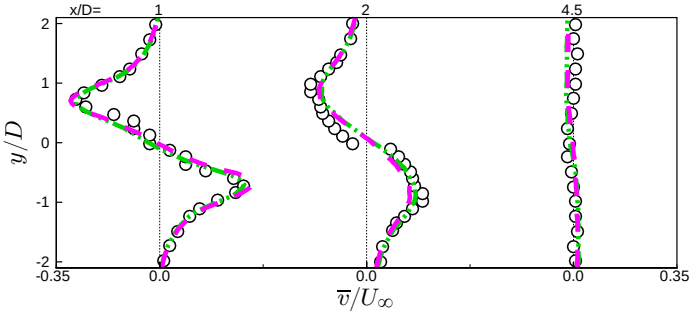

(a) Time-averaged velocity v

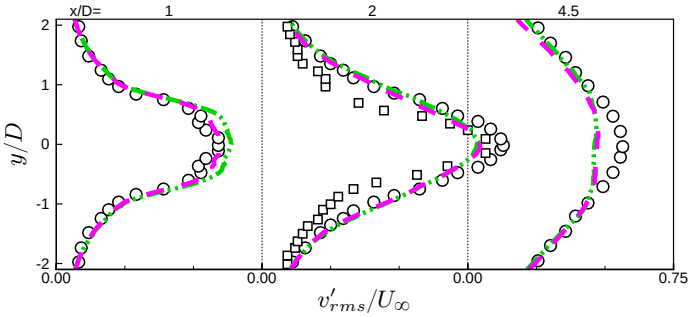

(b) RMS fluctuation of velocity v

Figure 12: Time-averaged transverse velocity and fluctuation profiles in the wake. —··— 4MSA, – – 4M$k\omega$, ○ Lyn et al. [21], □ Fohanno & Martinuzzi [22].

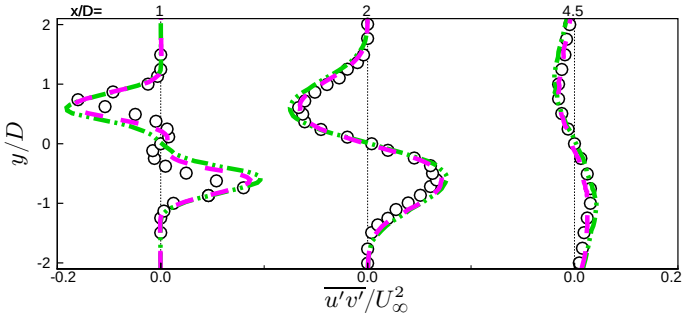

Figure 13: Reynolds stress $\overline{u'v'}$ in the wake. –·–· 4MSA, – – 4M$k\omega$, ○ Lyn et al. [21].

4.1.3. Time-averaged surface convective heat transfer

The convective heat transfer on cylinder surfaces is validated by the global and local Nusselt number. Table 3 summarises the time-averaged global Nusselt number of the present cases and three other studies. Results of case 4M$k\omega$ and 8M$k\omega$ are much closer to that of the experiments with only about 5% error compared to 14% from the 4MSA case and 18% from the 1M$k\omega$ case. More detailed validation is conducted using the time-averaged local Nusselt number profiles on cylinder surfaces as illustrated in Fig. 14. Profiles of 4 cases agree well with experiments on the front surface AB. The Nusselt number of the 8M$k\omega$ case on the front surface is lower than that of the 4M$k\omega$ case. This is the main reason of the lower global Nusselt number of the 8M$k\omega$ case compared to that of the 4M$k\omega$ case although profile of the 8M$k\omega$ case is closer to the experimental data. On the top surface BC and bottom surface DA, underestimate occurs in case 1M$k\omega$, 4MSA and 4M$k\omega$ soon after the front corner B and A while the profile of 8M$k\omega$ follows the experimental profiles closely. It is believed that the underestimate of the reverse flow velocity in the near-wall region, although very small in the velocity profiles above the cylinder top surface, is the main reason for the reduced surface heat transfer rate. The valley and peak of the heat transfer profile are more accurately captured by the 8M$k\omega$ case compared to that in the other cases due to the reduced surface grid spacing near the corners. On the rear surface CD, local Nusselt number of case 8M$k\omega$ and 4M$k\omega$ show good agreement with the experimental data while underestimate occurs in results of case 1M$k\omega$ and 4MSA. This is due to the underestimate of the reverse flow's kinetic energy in the near-wake as indicated by the wake velocity profiles. The results close to corner C and D are improved slightly in the 8M$k\omega$ case compared to the 4M$k\omega$ case which is also due to the improved local grid resolution.

Table 3: Global Nusselt number of simulations compared to experiments.

Data source	$\overline{Nu_g}$	Scheme
Igarashi [23]	107.6	Experiment
Yoo et al. [26]	109.4	Experiment
Boileau et al. [5]	101.6	LES wall-resolved
1M$k\omega$	88.2	LES-SST
4MSA	92.9	LES-SA
4M$k\omega$	102.4	LES-SST
8M$k\omega$	101.5	LES-SST

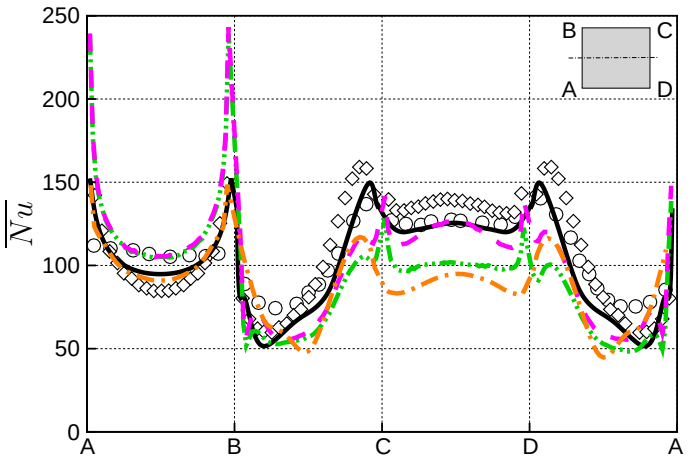

Figure 14: Time-averaged local Nusselt number on cylinder surfaces. –·– 1M$k\omega$, – – 4MSA, – – 4M$k\omega$, —— 8M$k\omega$, ○ Igarshi [23], ◇ Yoo et al. [26].

4.2. Phase-averaged results

4.2.1. Phase-averaged velocity profiles

The frequency of the vortex shedding is evaluated by FFT of the pressure signal. The 1M$k\omega$, 4MSA and 4M$k\omega$ cases report a Strouhal number of 0.134. This vortex shedding frequency agrees well with that of the experiments in Table. 2. Phase-averaged velocity profiles of case 4MSA and 4M$k\omega$ are examined for more detailed validation of how the flapping shear layer and wake vortex shedding are captured.

The streamwise velocity and the RMS fluctuation above the cylinder at selected phase angles are plotted in Figs. 15 and 16. The minimum and maximum distance of the shear layer to the top surface is reached at phase angle 90° and 270°, which is clearly illustrated by the velocity profiles at two phase angles. The velocity profiles of the 4MSA case agree well with that of the experiment at phase angle 270°. However, the upper bound of the shear layer in the 4MSA case is higher than that of the experiment and the 4M$k\omega$ case at phase angle 90°. Remarkably, profiles of the 4M$k\omega$ case match well with that of the experiment at both phase angles. It indicates that the shear layer near the top surface in the 4M$k\omega$ case is captured more accurately than that in the 4MSA case. The profiles of RMS fluctuation of both cases are close to that of the experiment. However, overestimate of the peak values can be found at

$x/D = 0.25$ in the 4MSA case at phase angle 90°. It suggests a higher unsteadiness in the shear layer above the cylinder top surface at $x/D = 0.25$ of the 4MSA case at phase angle 90° compared to that of the 4M$k\omega$ case and experiment. At phase angle 270°, profiles of both cases are close to the experiment despite slight discrepancies in the peak value.

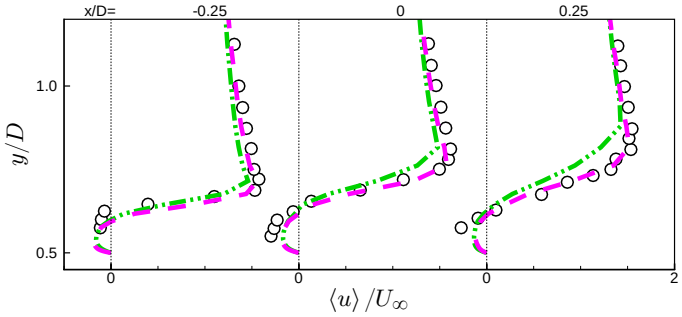

(a) Phase angle 90°

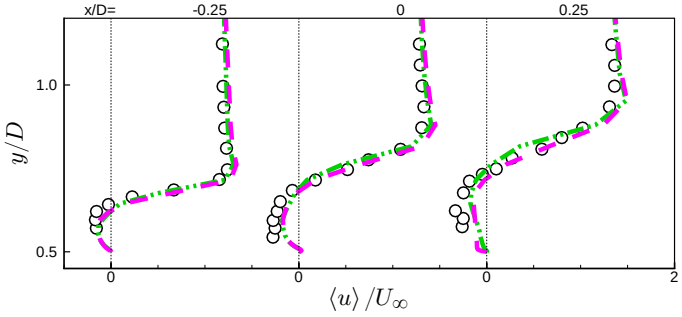

(b) Phase angle 270°

Figure 15: Phase-averaged streamwise velocity profiles above the cylinder at selected phase angles. —··— 4MSA, – – 4M$k\omega$, ○ Lyn & Rodi [20].

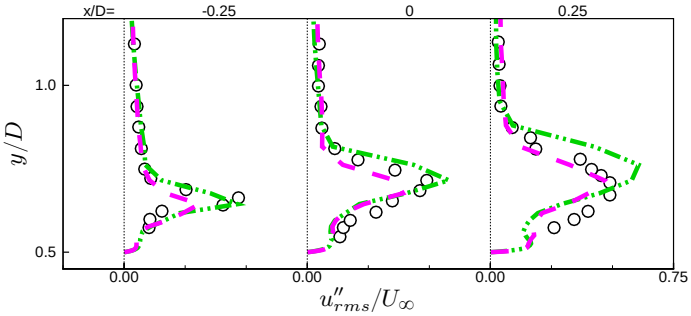

(a) Phase angle 90°

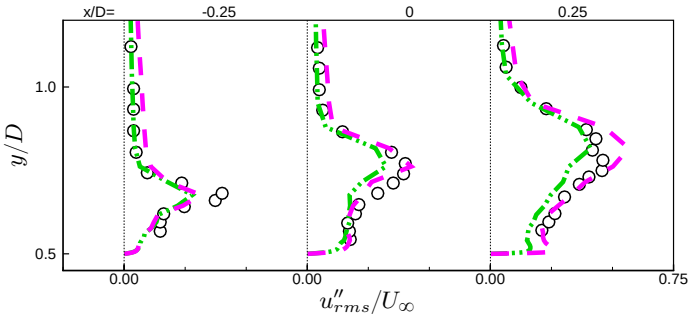

(b) Phase angle 270°

Figure 16: Phase-averaged streamwise velocity fluctuation profiles above the cylinder at selected phase angles. —··— 4MSA, – – 4M$k\omega$, ○ Lyn & Rodi [20].

Fig. 17 presents the phase-averaged streamwise and transverse velocity at $x/D = 2$ in the wake. Profiles of both cases show a similar variation and are close to the experimental data. Results of the streamwise velocity in the 4MSA case are a little overestimated. Meanwhile, lower values of the streamwise velocity are obtained from the 4M$k\omega$ case and they are closer to the measurements despite the amplitudes are slightly underestimated. For the transverse velocity, profiles of both cases agree well with that of the experiment outside the core region of wake vortices ($y/D \geqslant 1$). The amplitudes of the transverse velocity in the core region ($y/D \leqslant 0.5$) are underestimated by the 4MSA case in spite of a similar variation in phases. Profiles of the 4M$k\omega$ case show closer values in terms of peak and valley though the decrease at phase angle 90° and increase at 270° are slower than that in the experiment. The phase-averaged 2D turbulent kinetic energy k at $x/D = 2$ is illustrated in Fig. 18. Profiles of both cases agree with the experimental data away from the core region ($y/D \geqslant 1$). Inside the core region ($y/D < 1$), profiles of the 4MSA case do not match well with that of the experiment. In comparison to the 4MSA case, the 4M$k\omega$ case provides improved profiles in the core region, in spite of small overestimates of the peak values.

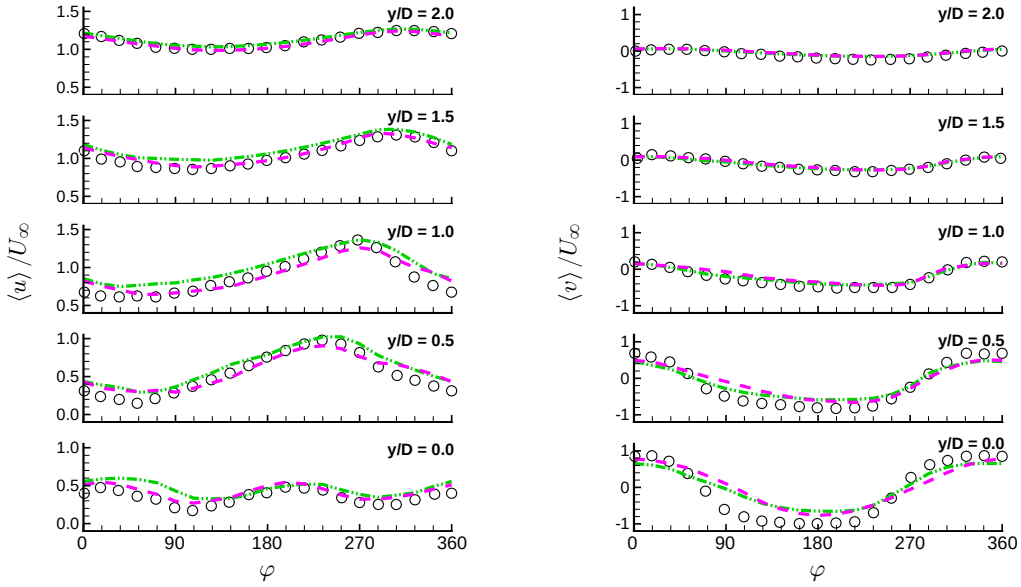

(a) Velocity u (b) Velocity v

Figure 17: Phase-averaged velocity profiles in the wake at $x/D = 2$. –·–· 4MSA, – – 4M$k\omega$, ○ Lyn et al. [21].

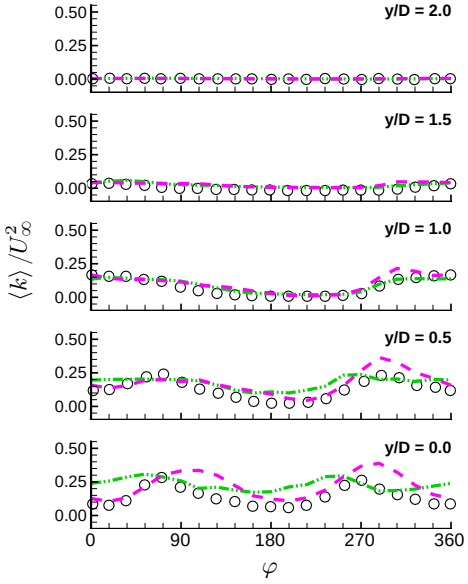

Figure 18: Phase-averaged turbulent kinetic energy profiles in the wake at $x/D = 2$. –·–· 4MSA, – – 4M$k\omega$, ○ Lyn et al. [21].

4.2.2. Phase-averaged surface convective heat transfer

Fig. 19 shows an overview of the phase-averaged local Nusselt number profiles in the 8M$k\omega$ case at selected phase angles. It is clearly shown that the value on the top/bottom surface, especially the downstream half, changes dramatically between phase angle 90° and 270°. This variation is closely related to the flapping movement of the shear layer. The upper bound of the shear layer moves close to the cylinder surface at 90° and the furthest distance to the surface is reached at 270°. The reverse flow sweeping on the top surface BC has different conditions at the two phase angles and therefore result

in different behaviour of heat transfer rate. Similarly, large variations of the local Nusselt number can be found on the rear surface except on the central part. This is mainly because of the large vortices growing and shedding close to the upper and lower half of the rear surface CD respectively. This shedding phenomenon brings changes to the flow pattern attached to the rear surface and thus influences the heat transfer rate on the surface. Profile on the front surface stays relatively unchanged except regions near the two corners.

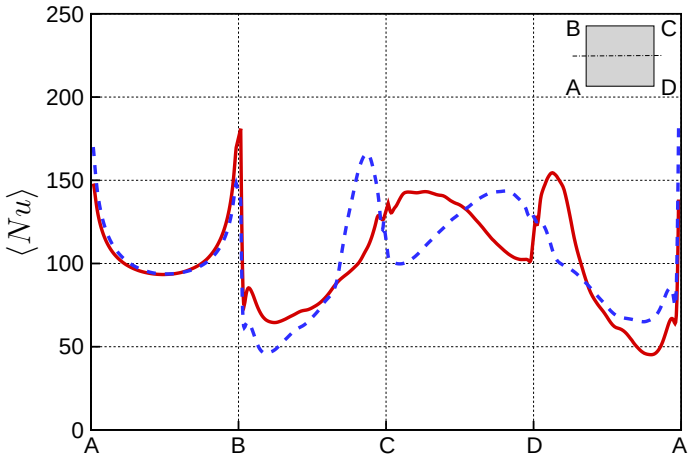

Figure 19: Phase-averaged local Nusselt number on cylinder surfaces at phase angle 90° (solid line) and 270° (dash line) of the 8M$k\omega$ case.

More detailed analysis is made with the phase-averaged local Nusselt number profiles at selected positions on top and rear surfaces illustrated in Fig. 20. The location of those points are also provided. Visible fluctuation of the local heat transfer rate is observed at point E, G and H. Profile of point E shows a maximum deviation of about 62% of the time-mean value from peak to valley. The difference between peak and valley at point F is greatly reduced due to its central position. But profile of point G shows a second high peak-to-valley variation of about 58% of the time-mean value. The rapid increase near phase angle 180° is due to the movement of the shear layer. From phase angle 90° to 270°, the upper boundary of the shear layer above the cylinder top surface moves away from a very close position. This expansion in the region inside the shear increases the amount of low temperature air sweeping on the top surface significantly. As a result, the convective heat transfer increases rapidly on point G during the expansion. In addition, the growing amount of air flow near point G causes a more serious stall of the heated flow upstream of point E because the growth of the region inside the shear layer is limited in the upstream location. This leads to a decrease of heat transfer rate near 180° at point E.

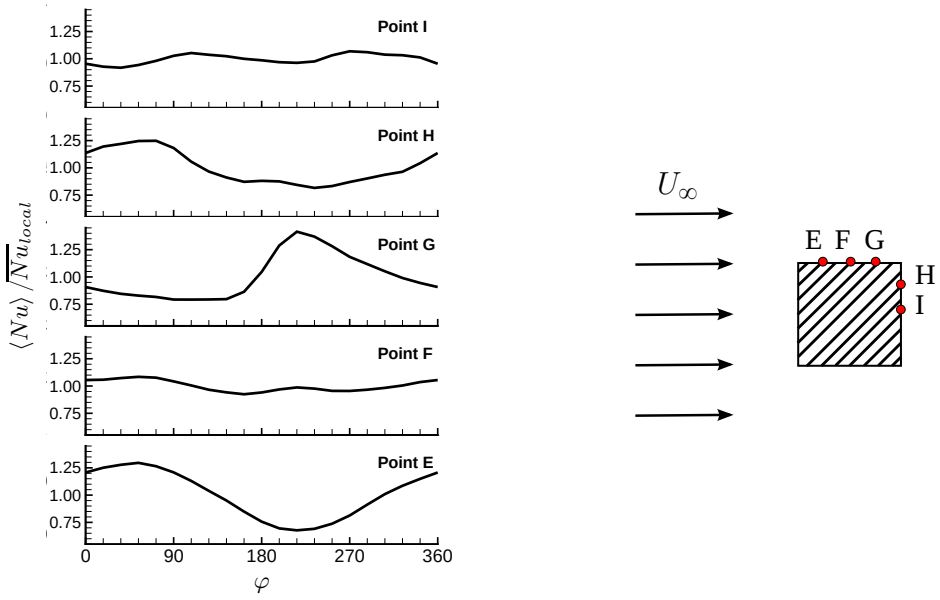

Figure 20: Phase-averaged local Nusselt number fraction at selected positions of the 8M$k\omega$ case.

The variation of local Nusselt number on the rear surface is illustrated by point H and I. The deviation of peak value from the valley is about 42% of the time-mean value at point H. The highest heat transfer rate on point H occurs between phase angle 0° and 90°. It is because that the formation of the vortex close to the upper part of rear surface brings low temperature air from the free stream above the cylinder. After the vortex is formed and starts shedding from phase angle 90° to 180°, the heat transfer rate drops at point H and as well as at point I. From phase angle 180° to 270°, the heat transfer rate at point I increases although the amplitude is rather small. This is because that the formation of the vortex close to the lower part of the rear surface brings low temperature air from the free stream on the bottom side of the cylinder. In the meantime, heat transfer rate at point H stays at a low level as the air flow passing the point is already heated by other part of the surface below point H. From phase angle 270° to 360°, development and shedding of the second vortex moves the stagnation point on the rear surface towards point H and therefore brings low temperature air that increases the heat transfer rate at point H. At central point I, the local heat transfer rate decreases due to the air flow passing through is already heated by other part of the surface near the stagnation point.

In the present unsteady case, the instantaneous surface convective heat transfer could be as much as 30% off the time-mean value. Such a large deviation could be vital to both the aerodynamic and thermal performances of engine components like turbine blades and combustor liners. It is important to accurately track and predict the peaks and valleys of the fluctuating surface temperature for the purpose of assessment and optimization and therefore reduce possible failures of such components.

4.3. Turbulent statistics

4.3.1. Spectral analysis

The spectra of turbulent kinetic energy (TKE), k, and pressure fluctuation, p', at several locations are presented in Figs. 21, 22, 23. Overall, the k spectra follow the Kolmogorov's 5/3 law in the inertial

subrange. Fig. 21 compares the spectra above the cylinder top surface from upstream to downstream. The power spectral density (PSD) of k stays low outside the recirculation region ($x/D = -0.5$). Details in the high frequency part ($f > 2 \times 10^3$) are missing at this position because the local flow field is dominated by the low frequency fluctuation related to the flapping shear layer. A clear increase in the PSD can be observed between the spectrum outside ($x/D = -0.5$) and inside the recirculation zone ($x/D \geqslant 0$). A small increase in the PSD occurs towards the wake region. It suggests that the TKE in the recirculation region have the highest PSD near the wake and reduces towards the upstream direction. The p' spectra show similar trends despite a much smaller increase in the PSD between $x/D = -0.5$ and $x/D = 0$.

Fig. 22 illustrates the spectra from near wall to outside the recirculation zone vertically at $x/D = 0$. An increase in the PSD can be found when the position moves away from the wall (from $y/D = 0.6$ to $y/D = 0.7$). Similar to $x/D = -0.5$ in Fig. 21, the PSD of k outside the recirculation zone ($y/D = 1.0$) drops significantly to a low level and only the low frequency part is active. The same applies to the spectra of p', though only a very small increase is found in the high frequency range ($10^3 < f < 10^4$) between the two profiles in the near-wall region.

The spectra of k and p' in the wake are presented in Fig. 23. The k spectrum decreases only in low ($f \leqslant 10^2$) frequency range from $x/D = 1$ to $x/D = 2$. This is because that the TKE in large scales (large vortices) is transported down to the small scales when moving towards downstream. The smallest vortices then dissipate into heat. At $x/D = 4$, the k spectrum drops in the whole frequency range. This is because that the energy continues transporting from the large scale to the small scale. As a result, the total TKE is decaying when moving downstream in the wake. This decay is also visible in the p' spectra but not as clear as in that of k.

It can be concluded from the spectra of TKE that the vortices are most energetic in the near-wake region ($x/D \approx 1$) where massive separation occurs due to the sudden expansion in the flow region after the rear corner. This is the main reason that the PSD of k increases in all frequency range from $x/D = 0$ to $x/D = 0.5$ in Fig. 21a. The vortices generated in the near-wake are then convected with the flow either to the recirculation zone or towards downstream of the wake. Turbulence decays naturally during the convection so the PSD of k reduces towards downstream in Fig. 23. In the recirculation region, turbulence is limited by the wall and thus lower PSD of k is observed at $y/D = 0.6$ compared to that at $y/D = 0.7$ in Fig. 22a. At locations outside the recirculation zone, the flow is dominated by the low frequency shear layer movement as the profiles in Figs. 21a and 22a illustrate.

Several peaks are shown in the spectra of k and p'. A strong peak in the p' spectra above the cylinder occurs at the vortex shedding frequency $f_{sh} = 505\ Hz$ corresponding to a Strouhal number of $St = 0.134$ in Figs. 21 and 22. Higher modes of the shedding frequency f_{sh} exist in the spectra but their energy is much lower than that at f_{sh}. However, the PSD of the higher modes in the wake region is increased to the same level of that at f_{sh} due to the quasi-symmetric nature of the shedding phenomenon. This makes it more difficult to distinguish the major frequency from higher modes in the wake region. In the k spectra, the PSD of the higher modes is comparable to that at f_{sh} in regions above the cylinder and in the wake. Therefore, the velocity signals are not suitable for the identification of vortex shedding

periods due to disturbances from higher frequency modes. It reveals the advantage of using the pressure signal on cylinder top surface in shedding phase identification is that this signal is not affected by the higher frequency modes.

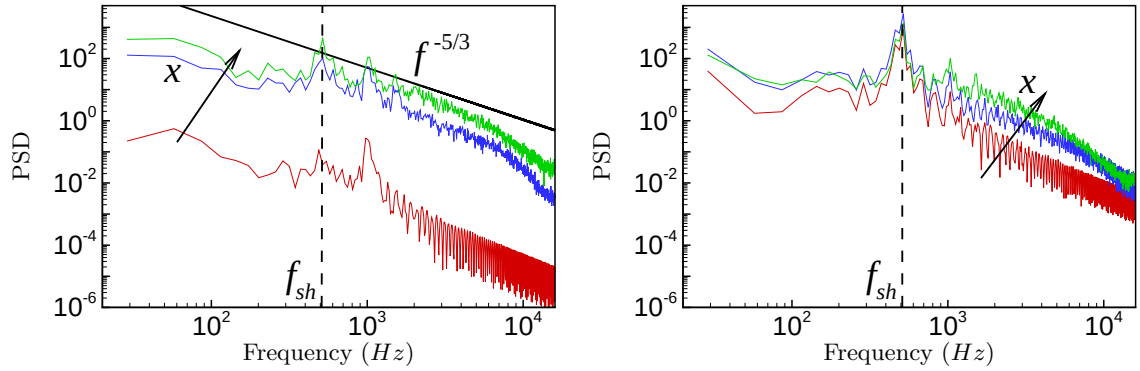

(a) Turbulent kinetic energy k (b) Pressure fluctuation p'

Figure 21: Spectra of k and p' above the cylinder at $y/D = 0.7$. red $x/D = -0.5$, blue $x/D = 0$, green $x/D = 0.5$.

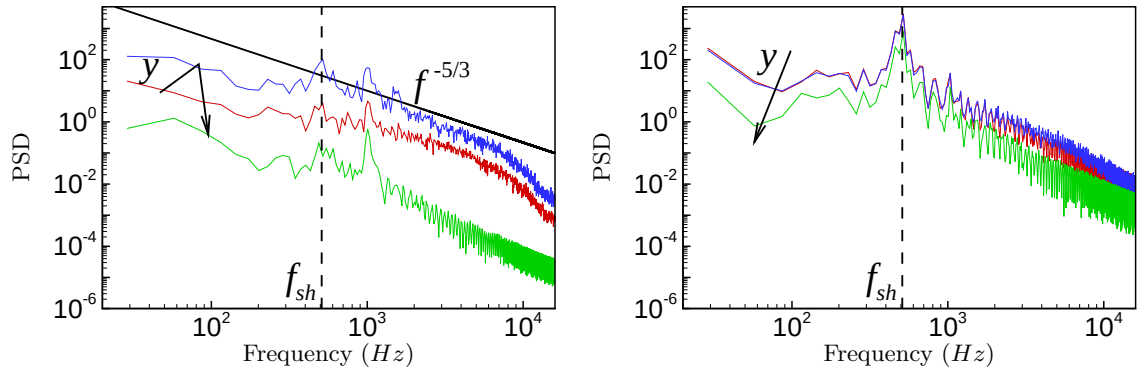

(a) Turbulent kinetic energy k (b) Pressure fluctuation p'

Figure 22: Spectra of k and p' above the cylinder at $x/D = 0$. red $y/D = 0.6$, blue $y/D = 0.7$, green $y/D = 1.0$.

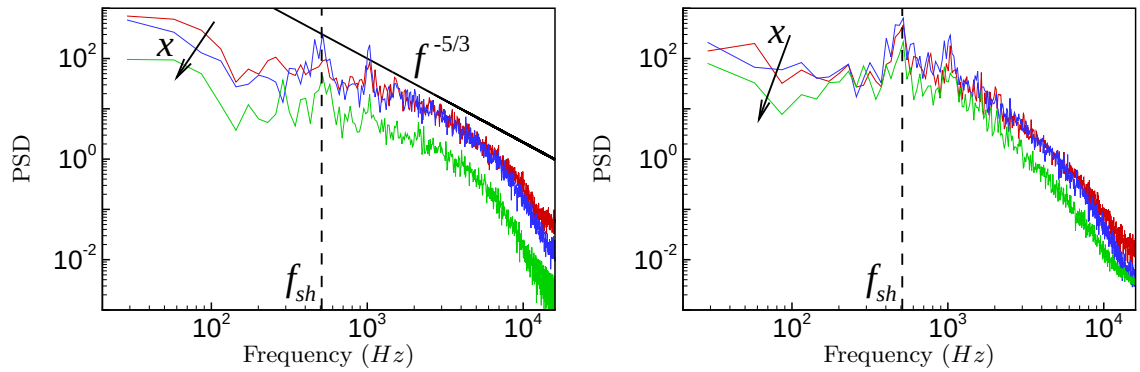

(a) Turbulent kinetic energy k (b) Pressure fluctuation p'

Figure 23: Spectra of k and p' in the wake at $y/D = 0.5$. red $x/D = 1$, blue $x/D = 2$, green $x/D = 4$.

4.3.2. Anisotropy of the Reynolds stress tensor

The state of the turbulence can be characterised by the anisotropy invariants that derived from the Reynolds stress tensor. This technique is first proposed by Lumley [29] in the study of return to isotropy of homogeneous turbulence using the normalised anisotropy tensor b_{ij},

$$b_{ij} = \frac{\langle u_i'' u_j'' \rangle}{2 \langle k \rangle} - \frac{1}{3}\delta_{ij} \tag{12}$$

in which k is the turbulent kinetic energy, "$\langle\rangle$" denotes the averaging process and u_i'' is the fluctuating velocity components. This tensor has a zero trace ($b_{ii} = 0$) and therefore it has only two independent invariants. In the present study, the two independent invariants are defined as,

$$\xi^2 = \frac{1}{6} b_{ij} b_{ji} \qquad \eta^3 = \frac{1}{6} b_{ij} b_{jk} b_{ki} \tag{13}$$

so that the left and right boundaries of the anisotropy invariant map (AIM) are two straight lines. The anisotropic state of the Reynolds stress tensor can be represented graphically in the AIM, often named as the Lumley triangle or the turbulence triangle. It has been demonstrated that all possible states of turbulence can be found within the Lumley triangle [29]. The 2D isotropic state of the turbulence, where the Reynolds stress vanishes in one direction and the other two being equal, is the top left corner of the Lumley triangle ($\eta = -\xi = 1/6$). The 1D turbulence, where only one direction of the Reynolds stress is none zero, locates at the top right corner ($\eta = \xi = 1/3$). The origin of the coordinates ($\eta = \xi = 0$) represents the 3D isotropic state. The straight line connecting the 3D isotropic state and 2D isotropic state is the negative axisymmetric line ($\eta = -\xi$), where the Reynolds stress is equal in two directions and greater than the third one. The straight line connecting 3D isotropic state and 1D turbulence is the positive axisymmetric line ($\eta = \xi$), where the Reynolds stress is equal in two directions but smaller than the third one. The curved line on top of the Lumley triangle between the 2D isotropic state and 1D turbulence corresponds to the 2D state of the turbulence and is referred to as two-component line in the following analysis. An example of the Lumley triangle and possible states of turbulence is presented in Fig. 24.

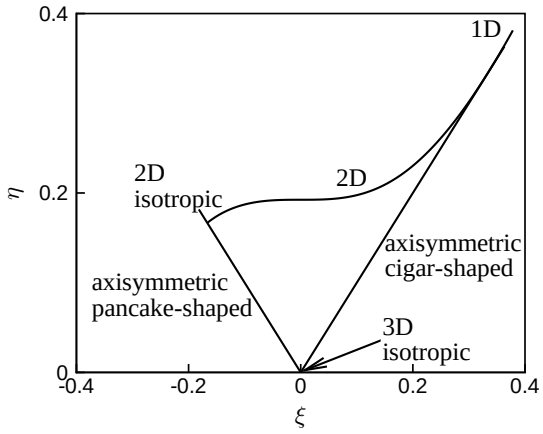

Figure 24: The Lumley triangle and possible states of turbulence in invariant coordiantes.

The anisotropy invariants at selected positions above the cylinder top surface and in the wake region are examined and discussed. Figs. 25 and 26 illustrate the phase-averaged flow field and anisotropic

state at selected points above the cylinder at phase angle 90° and 270° respectively. The invariants fall on the two-component line in the viscous sublayer (AB) at both phase angles. This is because that the production of turbulence normal to the wall is restricted by the effect of wall and thus the turbulence here is almost 2D. The invariants move slightly away from the two-component line as y^+ is increasing and it is better shown in the AIM at phase angle 270° because of the thicker boundary layer.

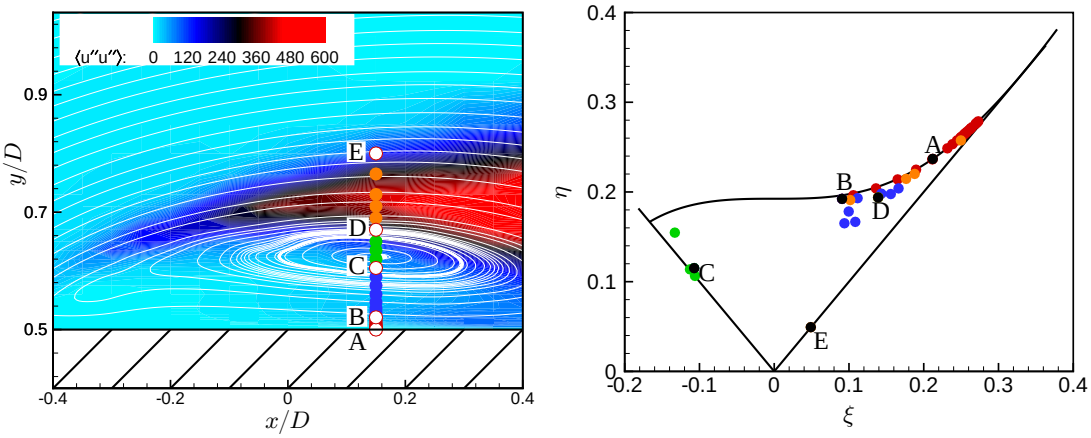

Figure 25: Phase-averaged flow field at phase angle 90° coloured by $\langle u''u'' \rangle$ (left) and the anisotropic invariant map (right) above the cylinder.

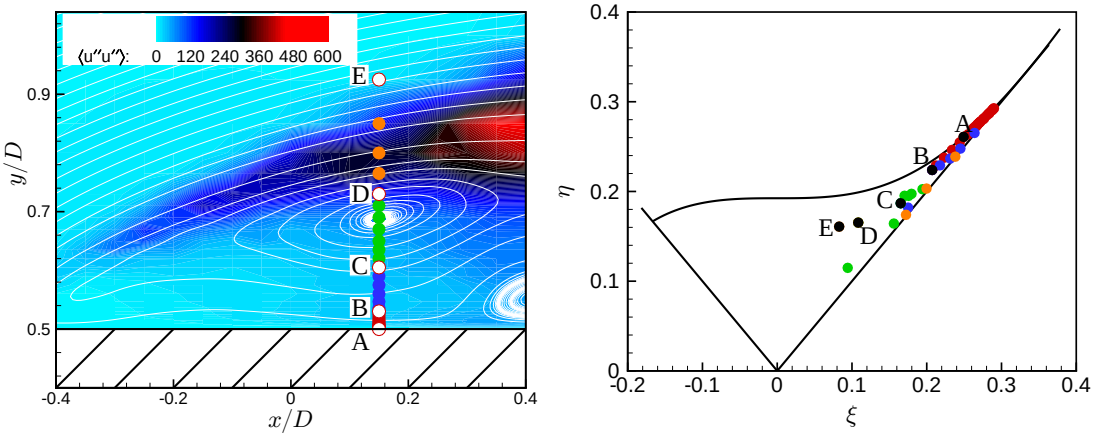

Figure 26: Phase-averaged flow field at phase angle 270° coloured by $\langle u''u'' \rangle$ (left) and the anisotropic invariant map (right) above the cylinder.

In the region between BC, the invariants reflect the state of the turbulence of the reattaching flow. The influence from the shear layer position is clearly seen at phase angle 90° as the invariants move off the two-component line but doesn't fall on the positive axisymmetric line as at phase angle 270°. In this region, the Reynolds stress is very small in y direction due to the restriction of wall and is relatively large in the x and z direction. A few points at phase angle 270° fall on the positive axisymmetric line. This is because that the shear layer is away from the wall at phase angle 270° and a small extension of the boundary layer region occurs. This distribution of invariants is similar to that in the boundary layer of a typical channel flow where the Reynolds stress in x and y directions is close to each other and much smaller than that in z direction.

In the region between CD, the invariants of the two phase angles locate close to the left and right boundary respectively. At phase angle 90°, the Reynolds stress in y direction is very small compared to the other two directions due to the compression of shear layer. Thus, the invariants fall in the left part near the negative axisymmetric line. At phase angle 270°, the Reynolds stress in y direction is greater than that at phase angle 90° and it is comparable to the x component. As a result, the invariants are located close to the positive axisymmetric line. Similar distribution is observed by Choi & Lumley [30] in axisymmetric contraction and expansion flows. They state that the energy ellipsoid of the homogeneous turbulence after the axisymmetric contraction has a pancake shape and that after axisymmetric expansion has a cigar shape. The position of the invariants falls on the negative axisymmetric line in the contraction flow and on positive axisymmetric line in the expansion flow.

In the region across the shear layer (between DE), the Reynolds stress in the x direction is much larger than that in the other two directions. At phase angle 90°, the Reynolds stress in y direction is only about 5% of the x component while the z component is at a moderate level. Therefore the invariants locate very close to the two-component line. At phase angle 270°, the y component is comparable to the z component because the position is far from the wall while the x component is much greater than the other two. This makes the invariants locate close to the positive axisymmetric line except the point D and E. It is worth noting that at point E in phase angle 90°, the y component nearly equals to the z component and the x component is greatly reduced compared to that in the centre of the shear layer. Thus the invariants of point E locate very close to the 3D isotropy state.

The state of turbulent above the cylinder top surface in the recirculation region is mainly influenced by the wall restriction and shear layer position. Similarities can be found inside the near-wall boundary layer. Opposite states of local turbulence occur in region CD where probes locate across the centre of the vortex. This reflects the effect of shear layer and its position on the state of the turbulence inside the recirculation region. In regions across the shear layer, state of local turbulence is slightly different between the two phase angles although the x components of the Reynolds stress dominates. This difference is also caused by the position of the shear layer which further affects the y component of the Reynolds stress.

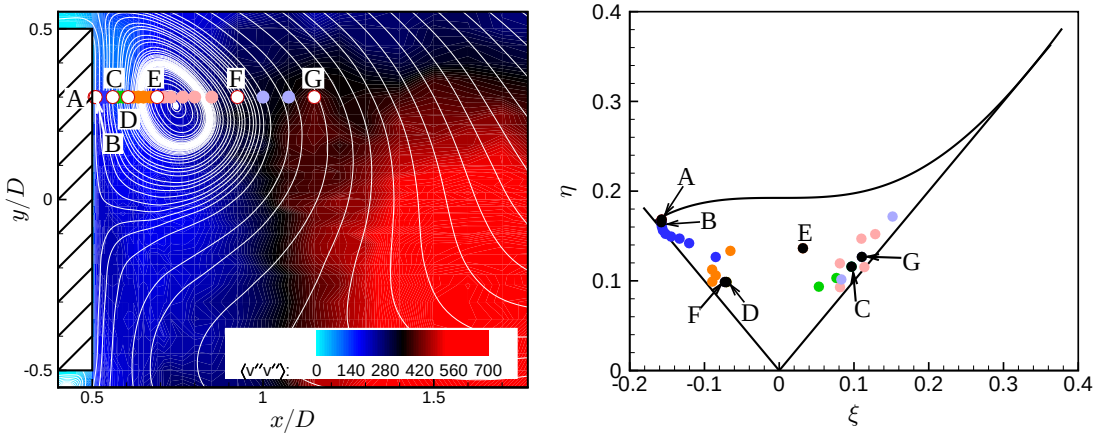

Figure 27: Phase-averaged flow field at phase angle 90° coloured by $\langle v''v'' \rangle$ (left) and the anisotropic invariant map (right) in the wake.

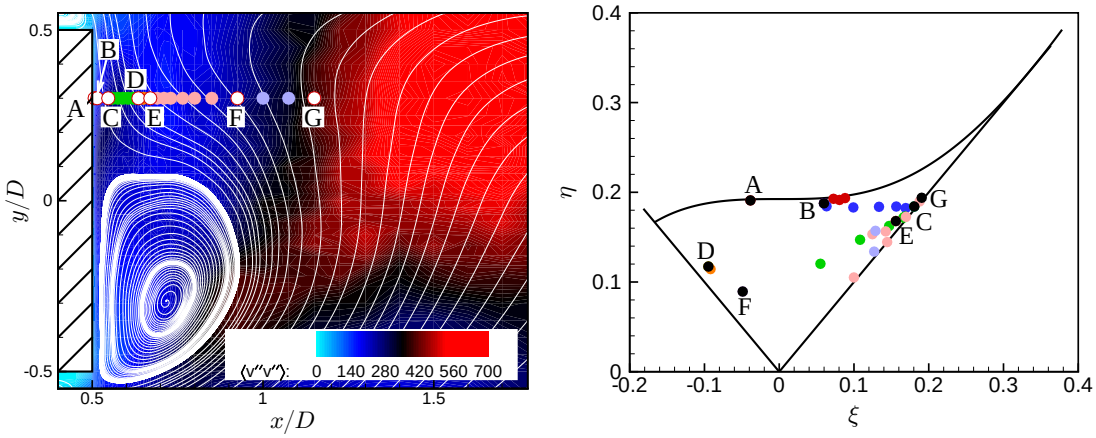

Figure 28: Phase-averaged flow field at phase angle 90° coloured by $\langle v''v'' \rangle$ (left) and the anisotropic invariant map (right) in the wake.

Figs. 27 and 28 present the phase-averaged flow field and anisotropic state at selected points in the wake of phase angle 90° and 270°. In the near-wall region (AB), the Reynolds stress is limited in the direction normal to the wall and invariants of both phase angles locate on the two-component line. The invariants move away from the two-component line as the position moves outside the viscous sublayer. At phase angle 90°, the Reynolds stress in y direction is close to that in z direction and is 10 times greater than the x component. This results in the location of invariants very close to the 2D isotropic state. At phase angle 270°, the x component of the Reynolds stress is greater than that at phase angle 90° and the y component is greater than the other two. As a result, the invariants fall in the positive half of the Lumley triangle. In the region between BC, the x component is increasing when moving away from the wall. Therefore, the invariants of both phase angles are moving towards the positive axisymmetric line.

In the region between CD, the Reynolds stress in y direction is slightly larger than the other two and the x component keeps growing. This results in the invariants moving down the map towards the isotropic state. However, the Reynolds stress in x direction becomes greater than that in z direction and close to the y component. A jump to the left part of the map is therefore observed in the AIM at point D.

In the region between DE, both the x and y components are growing but the y component is growing faster than the x component. This is because that the position is moving towards vortex centre at phase angle 90°. It induces a smooth transition of the invariants from the left to the right part in the Lumley triangle. The situation is slightly different at phase angle 270° as the probe is moving downstream in the separating/reattaching flow. This is probably the reason of a sudden jump from the left to the right part in the Lumley triangle and the region is much smaller than that at phase angle 90°.

Between point E and F, the y component dominates the Reynolds stress and the invariants locate close to the positive axisymmetric boundary. The x component of the Reynolds stress increases after the centre of the vortex at phase angle 90°. At phase angle 270°, the position continues moving downstream towards the second vortex. This results in point F being located in the left part of the Lumley triangle. Afterwards, it is moving towards the second vortex at both phase angles and the x component is reducing. The points after point F locate close to the positive axisymmetric line.

The state of the turbulence in the near-wake region is different between phase angle 90° and 270° owing to the different flow pattern. At phase angle 90°, probes locate across the vortex formed near the upper half of the rear surface. The x component of the Reynolds stress is limited both by the wall and the vortex before point E and invariants concentrate on the left half of the Lumley triangle. The x component increases considerably after point E and invariants group on the right half of the Lumley triangle. At phase angle 270°, the vortex forms near the lower half of the rear surface. The probes before point E represents the state of the turbulence of the reattaching flow and those after point E illustrates the state of the turbulence affected by separation.

A conclusion can be drawn from the previous analysis that the local state of the turbulence in the near-wake region is influenced not only by the restriction of the wall, but also affected by the vortex shedding and separation/reattachment. The boundary layer attached to the rear surface is relatively thin compared to that of the flow near the cylinder top surface. Different distributions of invariants are shown between the region across the vortex (phase angle 90°) and the region with reattachment and separation (phase angle 270°).

4.4. Phase indentification by proper orthogonal decomposition

POD has been a popular tool in the analysis of coherent structures in unsteady flows since it being introduced first by Lumley [31] in the study of turbulence. However, it is difficult for the traditional POD method to deal with large datasets obtained from experiment or simulation. In order to reduce the amount of calculation required by POD, Sirovich [32] proposed a "snapshot POD method" and it has been widely used in recent studies [33, 34]. Oudheusden et al. [35] investigate the phase-averaged flow field in the wake of a 2D square cylinder at incidence. The 2D snapshot POD analysis is applied to velocity data obtained by means of particle image velocimetry (PIV). The phase of each individual dataset is determined from the first pair of POD modes. It is found that the reconstructed flow field from the mean flow and first pair of POD modes compares well with the conventional phase-averaged flow field. Perrin et al. [36] have studied the flow passing a circular cylinder at high Reynolds number. The fluctuating velocity field reconstructed from the POD modes is analysed and it is discovered that the first 2 modes are the best in determining the phase of the vortex shedding. A phase jitter occurs between the pressure signal and velocity signal. This results in an overestimate of the random part of the motion by using the conventional pressure-signal method. This effect is alleviated by the use of POD modes in phase identification.

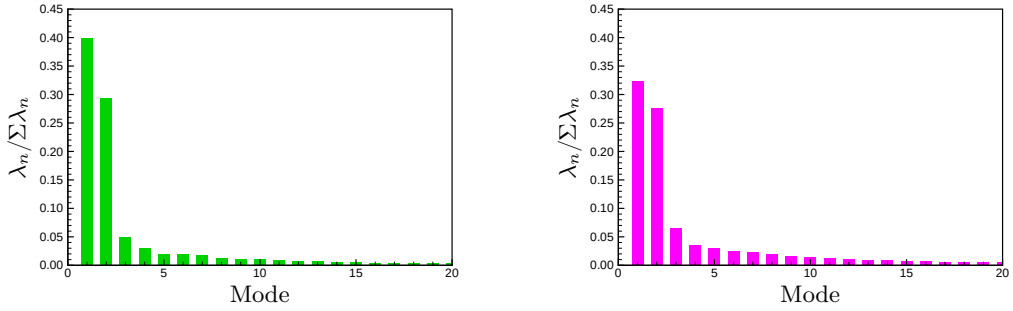

(a) 4MSA (b) 4M$k\omega$

Figure 29: Eigenvalue fractions of the first 20 POD modes of the 2 cases.

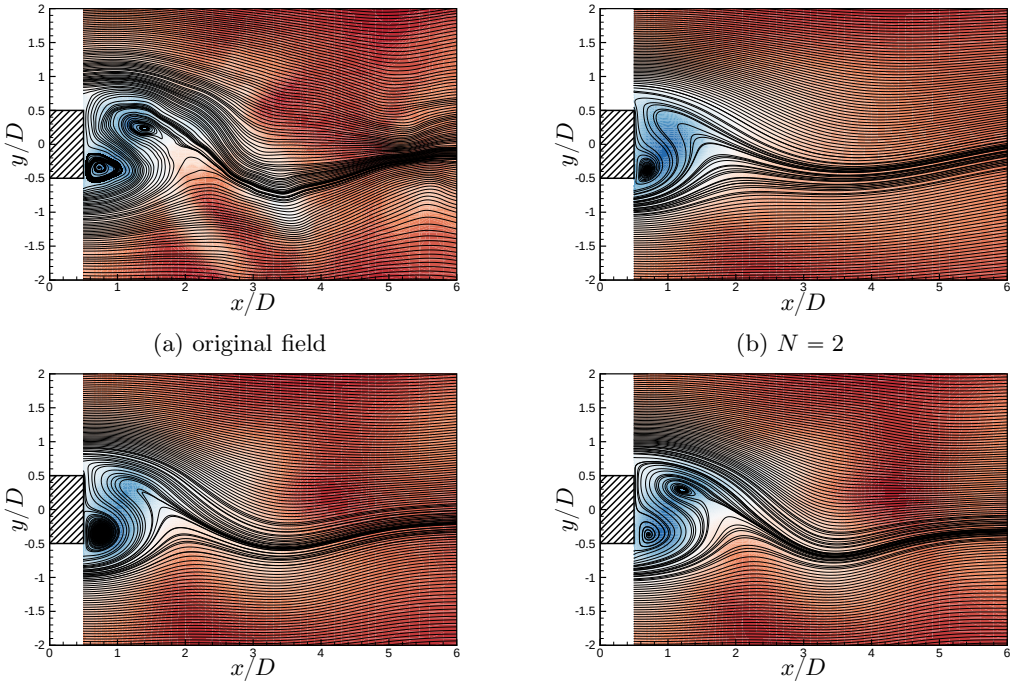

(a) original field (b) $N = 2$

(c) $N = 10$ (d) $N = 20$

Figure 30: Instantaneous flow field coloured by pressure at $t = 0.0159s$ reconstructed by the first N POD modes of the 4M$k\omega$ case.

2D snapshot POD analysis is applied to 5,500 snapshots of the velocity field obtained from case 4MSA and 4M$k\omega$. Fig. 29 presents the eigenvalue fraction of the first 20 POD modes in both cases. Similar to Oudheusden et al. [35] and Perrin et al.[36], the first 2 POD modes occupy a total of 70% and 60% of the total turbulent kinetic energy respectively. Fig. 30 shows the reconstructed instantaneous flow field and pressure contours from different POD modes in the 4M$k\omega$ case. The first 2 modes have captured the major vortices in the wake region. More accurate prediction of the second vortex in the wake that sheds from the cylinder is achieved by the 10-mode and 20-mode reconstructions. In the present study,

the first 2 POD modes are sufficient for the identification of the phase angle of each snapshot following,

$$\mathbf{u}(\mathbf{x},t) = \langle \mathbf{u}(\mathbf{x},\varphi)\rangle + \mathbf{u}''(\mathbf{x},t)$$

$$\langle \mathbf{u}(\mathbf{x},\varphi)\rangle = \overline{\mathbf{u}}(\mathbf{x}) + c_1(\varphi)\cdot\phi_1(\mathbf{x}) + c_2(\varphi)\cdot\phi_2(\mathbf{x})$$

$$\mathbf{u}''(\mathbf{x},t) = \sum_{i=3}^{N} c_i(\varphi)\cdot\phi_i(\mathbf{x}) \tag{14}$$

$$\frac{c_1(n)}{\sqrt{2\lambda_1}} = r_n\sin(\varphi_n) \qquad \frac{c_2(n)}{\sqrt{2\lambda_2}} = r_n\cos(\varphi_n) \qquad {r_n}^2 = \frac{c_1(n)^2}{2\lambda_1} + \frac{c_2(n)^2}{2\lambda_2} \tag{15}$$

where φ is the vortex shedding phase angle, n is the index of snapshots, i is the index of POD modes and λ_i is the eigenvalue of the corresponding POD mode.

The representation of the orthogonal components of the first 2 modes is verified by the cross plot of the normalised coefficients as Fig. 31 shows. The ideal circumstance is given by a circle in the normalized (c_1, c_2) plane, while the scatter of the data points is an indication of the unsteady vortex shedding cycles. The phase angle of each snapshot n is calculated from,

$$\tan(\varphi_n) = \frac{c_1(n)\sqrt{2\lambda_2}}{c_2(n)\sqrt{2\lambda_1}} \tag{16}$$

After the phase angle of each snapshot is identified, the ensemble dataset can be averaged according to the phase angles of the vortex shedding period. This phase-averaging process is named as POD based phase identification method ("POD based method") in comparison to the conventional pressure-signal based phase identification method ("pressure based method").

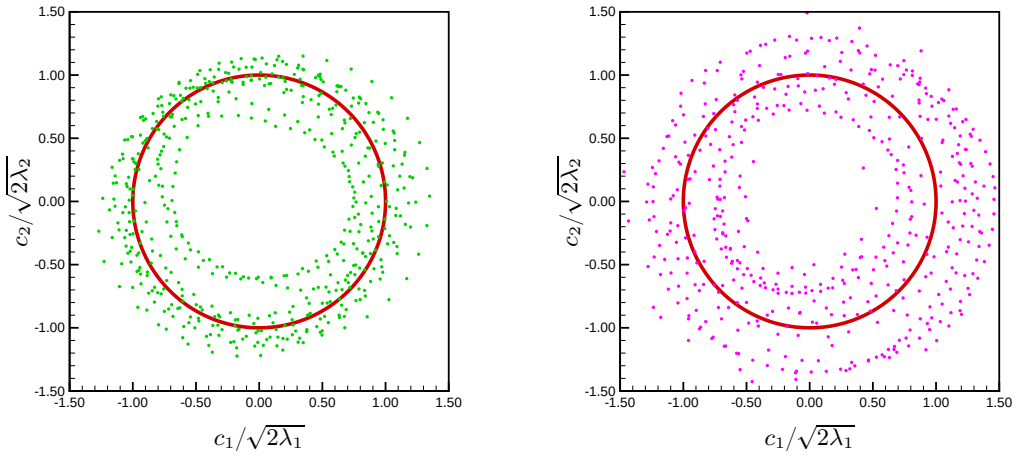

(a) Case 4MSA (b) Case 4M$k\omega$

Figure 31: Coefficient correlation of the snapshots from the 2 cases.

Validation of the POD based method is done by comparing the phase-averaged velocities to that of the pressure based method and experiment. Profiles of the 4MSA case are presented in Fig. 32. Results of the POD based method are closer to the experimental data compared to the pressure based method. The greater fluctuation of velocity in phases shows that the POD based method is more accurate in capturing the shedding of vortices in the wake. Meanwhile, the pressure based method underpredicts the velocity variation in phases in the wake region especially in the core region ($y/D \leqslant 1.0$). Results of the

two methods in the 4M$k\omega$ case are presented in Fig. 33. It shows that the POD based method captures the vortex movement in the wake better than the pressure based method in the core region ($y/D \leqslant 1.0$) despite slight overestimate of the valley of streamwise velocity when $\varphi \leqslant 90^\circ$. The base line value of the phase-averaged streamwise velocity of the POD based method away from the core region ($y/D \geqslant 1.5$) is slightly overestimated.

The reason that the improvement of POD based results of the 4M$k\omega$ case are not as good as that of the 4MSA case is probably due to the less energy contained in the first 2 POD modes. As a result, the identification of phase angles that associated with the coherent structures in the 4M$k\omega$ case is not as clear as that in the 4MSA case. It can be concluded that the quality of POD, especially how well the first 2 modes have identified the major vortices, is directly linked with how well the phase-averaged results could be in the POD based method.

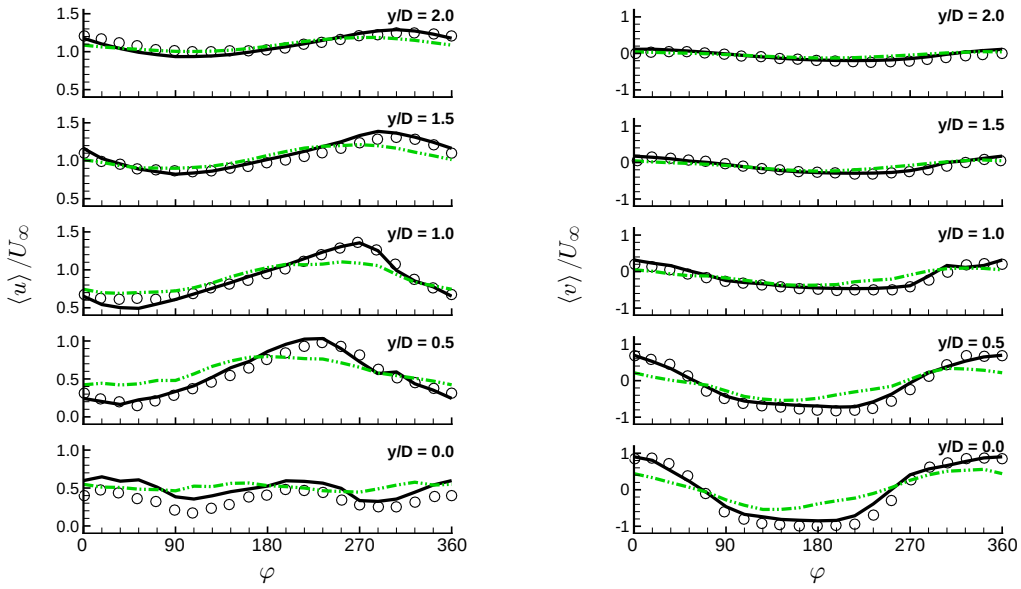

(a) Velocity u (b) Velocity v

Figure 32: Phase identification by POD: phase-averaged velocity profiles in the wake at $x/D = 2$ of 4MSA. —·— pressure based method, —— POD based method, ○ Lyn et al. [21].

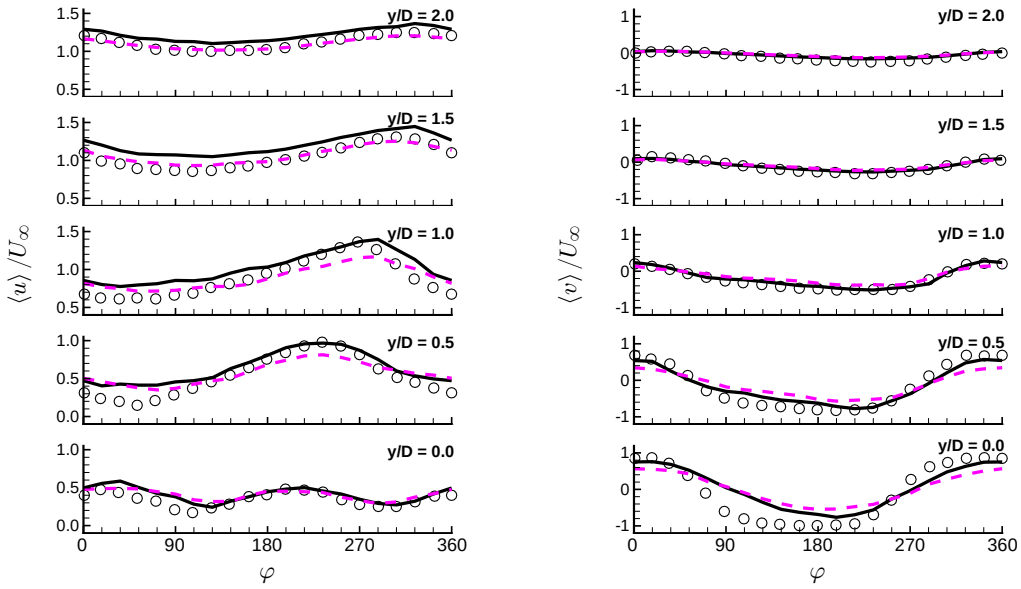

(a) Velocity u (b) Velocity v

Figure 33: Phase identification by POD: phave-varying velocity profiles in the wake at $x/D = 2$ of 4M$k\omega$. – – pressure based method, —— POD based method, ○ Lyn et al. [21].

5. Conclusions

A hybrid LES-RANS approach is successfully applied to the unsteady heat transfer study of a heated square cylinder in cross flow. Both the LES-SA and LES-SST approaches have captured the time-averaged flow field based on a modest 4-million-cell grid. The LES-SST approach shows clear advantages over the LES-SA approach in predicting the surface heat transfer, especially on the rear surface of the cylinder, owing to the better resolved near-wake vortices. Grid convergence study demonstrates that more accurate predictions can be obtained on surface heat transfer with increased grid resolution in key regions on cylinder surfaces and in the near-wake.

Phase-averaging based on the pressure-signal on cylinder top surface reveals time varying behaviours of the flow field. Velocity profiles of the LES-SST approach agree better with the measured data compared to that of the LES-SA approach. The variation of local surface heat transfer against vortex shedding phases is illustrated for all surfaces and selected local positions. It is found that a maximum variation of 30% of the time-mean value occurs locally on the cylinder surfaces. This demonstrates the importance to have accurate prediction of the time- or phase-varying surface temperature in highly unsteady flows.

The analysis of turbulent statistics shows some insights into the unsteady flow field. The spectra of k and p' suggest that the energy mainly comes from the flapping shear layer and vortex shedding. This energy is then fed into recirculating flows above and below the cylinder and vortices in the wake. The main vortex shedding frequency can be captured from the p' spectra on top of the cylinder. However, it mixes with higher frequency modes in the k and p' spectra in the wake. This shows the effectiveness of using the p' signal from the cylinder top surface for shedding phase determination in a conventional pressure method.

The state of the turbulence in regions above the cylinder top surface and in the near wake is studied using the anisotropy invariants of the Reynolds stress tensor. It can be concluded that the state of the turbulence above the cylinder is governed by the restriction of the wall and the flapping shear layer. However, contributions to the state in the near-wake consists of not only the restriction of the wall, but also strong effects from shedding vortices and the separation/reattachment. The complex interaction makes the state of the turbulence vary significantly across different near-wake regions and phase angles.

The identification of shedding phase angles directly from the velocity field in the wake using POD is shown to be promising. The phase angle of each snapshot is defined based on the first 2 modes of the POD, which occupies $60 \sim 70\%$ of the total TKE. Better phase-averaged velocity profiles in the wake are obtained compared to the conventional pressure-signal method. It is found that the quality of POD, especially that of the first 2 modes, has a strong influence on phase-averaged velocities.

6. Acknowledgment

The authors would like to acknowledge the use of the "Hydra" High Performance Computing System at Loughborough University. Support from the Department of Aeronautical and Automotive Engineering and the Rolls-Royce UTC is kindly appreciated.

Nomenclature

Δt	time step
Δ	filter (grid) width (= $\max(\Delta x, \Delta y, \Delta z)$)
δ_{ij}	Kronecer delta
κ	thermal conductivity
κ_T	turbulent conductivity
λ_{prism}	growth rate of the prism layers
$\mathbf{F}$	flux vector
$\mathbf{F}^{inv}$	inviscid flux vector
$\mathbf{F}^{vis}$	viscous flux vector
$\mathbf{Q}$	conservative vector
μ	molecular viscosity
μ_T	turbulent eddy viscosity
μ_T	turbulent viscosity
ν	kinematic viscosity
ω	specific dissipation rate
ρ	fluid density
τ_{ij}	stress tensor
φ	phase angle of the vortex shedding
$\widetilde{\nu}$	kinematic eddy viscosity
$\widetilde{d}$	modified wall distance
C_{DES}	DES model constant
C_p	pressure coefficient
c_p	specific heat
D	cylinder diameter
d	distance to the nearest wall
d_c	RANS cut-off distance
E	total energy
e	internal energy
k	turbulent kinetic energy
M	Mach number
N_{cell}	total cell number
N_{prism}	total prism layer
Nu	Nusselt number
p	static pressure of the fluid
Pr	Prandtl number
q_i	Cartesian components of heat flux $\mathbf{q}$
R	gas constant
Re	Reynolds number
S_{ij}	strain-rate tensor
Sc	Schmidt number
Sh	Sherwood number
St	Strouhal number
T	temperature
t	physical time
t^*	convective time
T_{total}	total physical time
Tu	turbulence intensity
u_i	Cartesian components of velocity $\mathbf{U}$
x_i	Cartesian coordinates
y^+	dimensionless wall distance

Subscripts

∞	inflow condition
exp	experimental value
g	global-averaged value
L/R	immediate left/right of the common face
rms	Root-mean-square value of the fluctuating part
sim	simulation value
T	turbulent value

Other Symbols

$\langle\rangle$	phase-averaged quantity
$\overline{()}$	time-averaged quantity
$\widetilde{()}$	Favre-filtered quantity
$''$	fluctuating part from phase-averaged value
$'$	fluctuating part from time-averaged value

References

[1] G. Bosch, W. Rodi, Simulation of vortex shedding past a square cylinder near a wall, Int. J. Heat and Fluid Flow 17 (3) (1996) 267–275. doi:10.1016/0142-727X(96)00033-1.

[2] G. Bosch, W. Rodi, Simulation of vortex shedding past a square cylinder with different turbulence models, Int. J. Numer. Meth. Fl. 28 (4) (1998) 601–616. doi:10.1002/(SICI)1097-0363(19980930)28:4<601::AID-FLD732>3.0.CO;2-F.

[3] W. Rodi, J. Ferziger, M. Breuer, M. Pourquiée, Status of large eddy simulation: Results of a workshop, J. Fluids Eng. 119 (2) (1997) 248–262. doi:10.1115/1.2819128.

[4] S. Wiesche, Large-eddy simulation study of an air flow past a heated square cylinder, Heat Mass Transfer 43 (6) (2007) 515–525. doi:10.1007/s00231-006-0122-x.

[5] M. Boileau, F. Duchaine, J. Jouhaud, Y. Sommerer, Large eddy simulation of heat transfer around a square cylinder using unstructured grids, AIAA J. 51 (2) (2013) 372–385. doi:10.2514/1.J051800.

[6] P. Spalart, W.-H. Jou, M. Strelets, S. Allmaras, Comments on the feasibility of les for wings and on a hybrid rans/les approach, in: C. Liu, Z. Liu (Eds.), Advances in DNS/LES, Columbus, OH: Greyden Press, 1997, pp. 137–147.

[7] M. Shur, P. Spalart, M. Strelets, A. Travin, Detached-eddy simulation of an airfoil at high angle of attack, in: W. Rodi, D. Laurence (Eds.), Engineering Turbulence Modelling and Experiments 4, Elsevier Science Ltd., 1999, pp. 669–678.

[8] N. Chauvet, S. Deck, L. Jacquin, Zonal detached eddy simulation of a controlled propulsive jet, AIAA J. 45 (10) (2007) 2458–2473. doi:10.2514/1.28562.

[9] A. Mitchell, S. Morton, J. Frosythe, R. Cummings, Analysis of delta-wing vortical substructures using detached-eddy simulation, AIAA J. 44 (5) (2006) 964–972. doi:10.2514/1.755.

[10] M. Barone, C. Roy, Evaluation of detached eddy simulation for turbulent wake applications, AIAA J. 44 (12) (2006) 3062–6071. doi:10.2514/1.22359.

[11] L. Davison, S. Peng, Hybrid les-rans modelling: A one-equation sgs model combined with a k-ω model for predicting recirculating flows, Int. J. Numer. Meth. Fl. 43 (9) (2003) 1003–1018. doi:10.1002/fld.512.

[12] P. Tucker, L. Davison, Zonal k-l based large eddy simulations, Comput. Fluids 33 (2) (2004) 267–287. doi:10.1016/S0045-7930(03)00039-2.

[13] P. Tucker, Novel miles computations for jet flows and noise, Int. J. Heat and Fluid Flow 25 (4) (2004) 625–635. doi:10.1016/j.ijheatfluidflow.2003.11.021.

[14] H. Xia, P. Tucker, S. Eastwood, Large-eddy simulations of chevron jet flows with noise predictions, Int. J. Heat Fluid Fl. 30 (6) (2009) 1067–1079. doi:10.1016/j.ijheatfluidflow.2009.05.002.

[15] H. Xia, P. Tucker, Numerical simulation of single-stream jets from a serrated nozzle, Flow Turbulence Combust. 88 (2012) 3–18. doi:10.1007/s10494-011-9377-5.

[16] P. Spalart, S. Allmaras, A one-equation turbulence model for aerodynamic flows, in: 30th Aerospace Sciences Meeting and Exhibit, Reno, NV, USA, 1992. doi:http://dx.doi.org/10.2514/6.1992-439.

[17] F. Menter, M. Kuntz, R. Langtry, Ten years of industrial experience with the sst turbulence model, in: K. Hanjalic, Y. Nagano, M. Tummers (Eds.), Turbulence, Heat and Mass Transfer 4, Begell House Inc., 2003, pp. 625–632.

[18] F. Menter, Improved two-equation k-ω turbulence models for aerodynamic flows, Tech. Rep. NASA TM 103975 (1992).

[19] H. Xia, Dynamic grid detach-eddy simulation for synthetic jet flows, dissertation, The University of Sheffield (2005).

[20] D. Lyn, W. Rodi, The flapping shear layer formed by flow separation from the forward corner of a square cylinder, J. Fluid Mech. 267 (1994) 353–376. doi:10.1017/S0022112094001217.

[21] D. Lyn, S. Einav, W. Rodi, J. Park, A laser-doppler velocimetry study of ensemble-averaged characteristics of the turbulent near wake of a square cylinder, J. Fluid Mech. 304 (1995) 285–319. doi:10.1017/S0022112095004435.

[22] S. Fohanno, R. Martinuzzi, A phase-averaged analysis of droplet dispersion in the wake of a square cylinder in a uniform stream, J. Fluids Eng. 126 (1) (2004) 110–119. doi:10.1115/1.1637637.

[23] T. Igarashi, Heat transfer from a square prism to an air stream, Int. J. Heat Mass Tran. 28 (1) (1985) 175–181. doi:10.1016/0017-9310(85)90019-5.

[24] P. Bearman, E. Obasaju, An experimental study of pressure fluctuations on fixed and oscillating square-section cylinders, J. Fluid Mech. 119 (1982) 297–321. doi:10.1017/S0022112082001360.

[25] S. Butterworth, On the theory of filter amplifiers, Exp. Wireless and Wireless Engineer 7 (1930) 536–541.

[26] S. Yoo, J. Park, C. Chung, M. Chung, An experimental study on heat/mass transfer from a rectangular cylinder, J. Heat Transfer 125 (6) (2003) 1163–1169. doi:10.1115/1.1603780.

[27] K. Cho, T. Irvine, J. Karni, Measurement of the diffusion coefcient of naphthalene into air, Int. J. Heat Mass Tran. 35 (4) (1992) 957–966. doi:10.1016/0017-9310(92)90260-Y.

[28] J. Jeong, F. Hussain, On the identification of a vortex, J. Fluid Mech. 285 (1995) 69–94. doi:10.1017/S0022112095000462.

[29] J. Lumley, Computational modelling of turbulent flows, Adv. Appl. Mech. 18 (1978) 123–176. doi:10.1016/S0065-2156(08)70266-7.

[30] K. Choi, J. Lumley, The return to isotropy of homogeneous turbulence, J. Fluid Mech. 436 (2001) 59–84. doi:10.1017/S002211200100386X.

[31] J. Lumley, The structure of inhomogeneous turbulence, in: A. Yaglom, V. Tatarski (Eds.), Atmospheric Turbulence and Wave Propagation, 1967, pp. 166–178.

[32] L. Sirovich, Turbulence and the dynamics of coherent structures. part i: Coherent structures, Q. Appl. Math. 45 (3) (1987) 561–570.

[33] K. Meyer, J. Pedersen, Oktayözcan, A turbulent jet in crossflow analysed with proper orthogonal decomposition, J. Fluid Mech. 583 (2007) 199–227. doi:10.1017/S0022112007006143.

[34] H. Chen, D. Reuss, V. Sick, On the use and interpretation of proper orthogonal decomposition of in-cylinder engine flows, Meas. Sci. Technol. 23 (8) (2012) 1–14. doi:10.1088/0957-0233/23/8/085302.

[35] B. van Oudheusden, F. Scarano, N. van Hinsberg, D. Watt, Phase-resolved characterization of vortex shedding in the near wake of a square-section cylinder at incidence, Exp. Fluids 39 (2005) 86–98. doi:10.1007/s00348-005-0985-5.

[36] R. Perrin, M. Braza, E. Cid, S. Cazin, A. Barthet, A. Sevrain, C. Mockett, F. Thiele, Obtaining phase averaged turbulence properties in the near wake of a circular cylinder at high reynolds number using pod, Exp. Fluids 43 (2007) 341–355. doi:10.1007/s00348-007-0347-6.